POLITECNICO DI MILANO

Faculty of Industrial Engineering

Master of Science in Space Engineering

VALIDATION OF A COMPLIANT STRUCTURE DESIGN PROCEDURE FOR A MORPHING TRAILING EDGE

Supervisor: Prof. Sergio Ricci

Co-supervisor: Eng. Alessandro De Gaspari

Master thesis by:

Alejandro Ortiz Ortega

Identification number: 780230

Academic year 2012-2013

to my family

Acknowledgments

Foremost, I would like to express my sincere gratitude to my supervisor Prof. Sergio Ricci from Politecnico di Milano for his guidance throughout and giving me the opportunity of collaborating in this project. Special mention goes to Ing. Alessandro De Gaspari from Politecnico di Milano for his time and assistance whenever I asked for it. I would not have been able to accomplish this task without his help.

The research leading to these results has gratefully received funding from the European Union Seventh Framework Programme (FP7/2007–2013) under Grant Agreement n. 284562.

A special thank goes to my friends both from Spain and Italy who have supported me throughout my life. In particular Raúl and Pedro with whom I have spent unforgettable moments.

I want to thank Irene for all that she has done and without whom these two years would not have been the same, neither would I.

Last but not least, I thank my family that has unconditionally and constantly supported me making me feel always close to them even when I have been far from home.

Ultimately, I thank all the people that have made of me the man I am now.

Abstract

This master thesis presents the work done for the optimization of a compliant structure for a trailing edge of a medium-range aircraft wing. The interest in morphing structures design for their implementation in modern aircrafts has increased in the latter years due to the fact that their use improves some certain performances, making a compromise between the load-carrying capabilities during flight and the weight reduction. In what follows, it has been adopted a two-level approach for the optimal design of morphing wings being the second level the main topic of this work, making used of a genetic algorithm in such a way to obtain the desired shape of the profile that will be implemented afterwards in the ribs of the wing of interest.

The work hereafter presented is placed in the framework of the European project SARISTU FP7 and has been focused on the research of the optimal configuration of the trailing edge for a given flight condition not only taking into account the efficiency of this kind of structures in providing the desired shape, but also the feasibility of such structures.

Key words: morphing wing, compliant structure, multiobjective optimization, genetic algorithm.

Sommario

In questa tesi si è affrontato il problema dell'ottimizzazione di una struttura a flessibilità distribuita lungo il bordo di uscita di un aereo di trasporto regionale. L'interesse nel progetto di strutture adattative per la successiva implementazione in aerei moderni è aumentato negli ultimi anni grazie al fatto che queste consentono un miglioramento di determinate prestazioni, arrivando ad un giusto compromesso fra la capacità di sopportare gli elevati carichi a cui gli aerei vengono sottoposti in volo e la riduzione di peso. L'approccio seguito per il progetto delle ali è costituito da due livelli. Il secondo livello costituisce l'argomento principale di questo lavoro. In questa seconda fase si cerca di ottimizzare una struttura a flessibilità distribuita mediante l'utilizzo di un algoritmo genetico in modo tale da ottenere le forme desiderate del profilo. In seguito queste soluzioni sono state implementate nelle centine dell'ala d'interesse.

Questo lavoro si inserisce nell'ambito del progetto europeo SARISTU FP7 ed è stato focalizzato sulla ricerca della configurazione ottima del bordo di uscita per una determinata condizione di volo, tenendo conto non solo dell'efficienza di questa tecnologia nell'ottenimento delle forme desiderate ma anche della fattibilità di questa soluzione.

Parole chieve: ala adattativa, struttura a flessibilità distribuita, ottimizzazione multiobiettivo, algoritmo genetico.

Resumen

Esta tesis de máster presenta el trabajo realizado para la optimización de una estructura a flexibilidad distribuida para el borde de salida de un ala de un avión de transporte regional. El interés por el diseño de estructuras adaptativas para su implementación en aeronaves modernas ha aumentado en los últimos años debido a que su uso permite una mejora en determinadas prestaciones, poniendo en compromiso la capacidad para soportar las altas cargas a las que una aeronave está sometida durante el vuelo con la reducción de peso. La estrategia seguida aquí para el diseño de tales alas adaptativas está constituida por dos niveles ocupándonos aquí del segundo nivel el cual trata de optimizar una estructura a flexibilidad distribuida mediante el uso de un algoritmo genético de forma tal que obtengamos la forma deseada del perfil, que luego será implementada en las costillas del ala que nos ocupa.

El trabajo realizado se enmarca en el ámbito del proyecto europeo SARISTU FP7 y se ha concentrado en la búsqueda de distintas configuraciones de borde de salida para una condición de vuelo dada no solo teniendo en cuenta la eficacia de esta tecnología en la obtención de la forma deseada, sino también en la factibilidad de dicha solución.

Palabras clave: ala adaptativa, estructura a flexibilidad distribuida, optimización multiobjetivo, algoritmo genético.

Contents

1 Introduction **1**

1.1 Morphing overview 2

1.2 Objectives 4

1.3 Outline 5

2 Multiobjective optimization of compliant mechanism using Genetic Algorithms **7**

2.1 Load path representation 7

2.1.1 Design variables 8

2.1.2 Parameters 10

2.1.3 Number of design variables 11

2.1.4 Finite Volume Beam models 12

2.2 Multiobjective optimization using Genetic Algorithms 13

3 Reference wing **19**

3.1 SARISTU FP7 project 19

3.2 Reference wing CAD 20

4 Morphing shapes and aerodynamic loads **23**

4.1 Airfoil shape representation (PHORMA) 23

4.1.1 The CST method 24

4.1.2 Representation of the morphing airfoil skin structural behavior . 27

4.2 Morphing configurations 28

4.2.1 Morphing leading edge 30

4.2.2 Morphing trailing edge 31

4.3 Load conditions 32

5 Synthesis of morphing airfoils **35**
5.1 Optimization problem formulation 35
5.2 Preliminary studies 37
5.2.1 Clamped trailing edge 39
5.2.2 Double material 42
5.2.3 Sliding constraint in the lower skin 45
5.2.4 Actuation in the lower skin sliding constraint 48
5.2.5 Conclusions 50
5.3 Multiobjective studies 50
5.3.1 Double material 52
5.3.2 Sliding constraint in the lower skin 53
5.3.3 Double material with sliding constraint in the lower skin 55
5.3.4 Conclusions 57

6 3D morphing wing validation studies **61**
6.1 Extension of the optimized solutions 62
6.2 First validation test 64
6.3 Second validation test 68
6.4 Conclusions 71

7 Conclusions **73**
7.1 Future developments 74

List of Figures

1.1 DIA-PoliMi rotative rib mechanism (left) and an adaptive compliant wing trailing edge flap (right). 4

2.1 A demonstrative connected load path representation of a SIMO compliant mechanism and the corresponding four types of characteristic points: active output points (cyan), deactivated output points (black) for the external load application, internal structure points (red), input actuation point (yellow) and constraint points (blue). 8
2.2 Optimal active points location for upper skin of inboard (left) and outboard (right) regions. 11
2.3 NSGA-II procedure. 14
2.4 Crowding distance calculation. 15

3.1 Structure of the activities taking place in the SARISTU project. 21
3.2 Morphing configuration of SARISTU reference wing CAD. 21
3.3 Procedure for the generation of morphing models. 22

4.1 The FrameWork PHORMA. 24
4.2 The geometric parameters describing the CST approach. 25
4.3 The Pascal triangle and the boundary conditions. 26
4.4 Procedure for the generation of morphing models. 29
4.5 SARISTU wing morphing configurations. 30
4.6 Aerodynamic studies of the reference wing for the trailing edge configuration. 33
4.7 Polar curves for the reference wing in the three trailing edge morphing configurations. 33

4.8 C_P comparison between EULER and XFOIL computations. 34

5.1 Selection of the sections of the reference SARISTU wing to be optimized. 37
5.2 Example of load paths corresponding to the initial population. 38
5.3 Shape change in the reference sections represented as CST objects. 38
5.4 Aerodynamic load for inboard region reference section (left) and outboard region reference section (right). 38
5.5 Pulling actuation solution for clamped trailing edge. Inboard region. . . 39
5.6 Pulling actuation solution for clamped trailing edge. Outboard region. . 40
5.7 Pushing actuation solution for clamped trailing edge. Inboard region. . 40
5.8 Pushing actuation solution for clamped trailing edge. Outboard region. 41
5.9 Inboard solution for single material clamped trailing edge. Dint in the lower skin. 41
5.10 Behavior of the LSE with respect to the skin Young's modulus variation. 43
5.11 Pulling actuation solution for trailing edge with different materials for skin and load paths. Inboard region. 43
5.12 Pulling actuation solution for trailing edge with different materials for skin and load paths. Outboard region 44
5.13 Pushing actuation solution for trailing edge with different materials for skin and load paths. Inboard region. 44
5.14 Pushing actuation solution for trailing edge with different materials for skin and load paths. Outboard region. 45
5.15 Pulling actuation solution for trailing edge with sliding constraint in the lower skin. Inboard region. 46
5.16 Pulling actuation solution for trailing edge with sliding constraint in the lower skin. Outboard region. 46
5.17 Pushing actuation solution for trailing edge with sliding constraint in the lower skin. Inboard region. 47
5.18 Pushing actuation solution for trailing edge with sliding constraint in the lower skin. Inboard region. 47
5.19 Solution for the case of input force actuating in the sliding constraint. Inboard region. 49
5.20 Solution for the case of input force actuating in the sliding constraint. Outboard region. 49

5.21 Double material solution for the case of double material configuration. Inboard region. 53
5.22 Double material solution for the case of double material configuration. Outboard region. 53
5.23 Equivalent deflection behavior for double material configuration. Inboard (left) and outboard (right). 54
5.24 Inboard solution for sliding constraint configuration. Pushing actuation. 54
5.25 Inboard solution for sliding constraint configuration. Pulling actuation. 55
5.26 Equivalent deflection behavior for slider and single material configuration. Pushing actuation (left) and pulling actuation (right). 55
5.27 Inboard solution for sliding constraint with different materials for skin and load paths. Pushing actuation. 56
5.28 Inboard solution for sliding constraint with different materials for skin and load paths. Pulling actuation. 57
5.29 Equivalent deflection behavior for slider and double material configuration. Pushing actuation (left) and pulling actuation (right). 57
5.30 Outboard solution for sliding constraint with different materials for skin and load paths and deflection behavior. 58
5.31 Pareto front plot for the different solutions. 59

6.1 Position of the adaptive ribs in the 3D wing. 61
6.2 Constraints application. 63
6.3 Attachment of the morphing trailing edge to the wing box by means of rigid elements RBE2. 63
6.4 Stringers in load paths connections with the upper skin. 64
6.5 Aerodynamic loads application. 64
6.6 Internal forces distribution in span-wise direction for Load Case 1. . . . 65
6.7 2D inboard solution for the first validation test. 65
6.8 2D outboard solution for the first validation test. 66
6.9 VonMisses stress $\left[\frac{N}{m^2}\right]$ contour plot for downwards deflection in the first validation. Inboard region (left) and outboard region (right). 67
6.10 Comparison of the displacements for the adaptive rib in station 4 according to different models of the first validation test. 67
6.11 VonMisses stress $\left[\frac{N}{m^2}\right]$ contour plot for structural requirement check in the first validation test. Inboard region (left) and outboard region (right). 68

6.12 Constraint force for mechanism locking in the first validation test. . . . 68
6.13 2D solution for the second validation test 69
6.14 VonMisses stress $\left[\frac{N}{m^2}\right]$ contour plot for downwards deflection in the second validation test. Inboard region (left) and outboard region (right). 70
6.15 Comparison of the displacements for the adaptive rib in station 4 according to different models of the second validation test. 70
6.16 VonMisses stress $\left[\frac{N}{m^2}\right]$ contour plot for structural requirement check in the second validation test. Inboard region (left) and outboard region (right). 71
6.17 Constraint force for mechanism locking in the second validation test. . . 71

List of Tables

4.1 Flight conditions given by Alenia. 32

5.1 Summary results for clamped solution. 42
5.2 Summary results for double material solution. 45
5.3 Comparison of input point displacement depending upon the performance of the actuation. 48
5.4 Summary results for sliding constraint solution. 48
5.5 Summary results for actuation in sliding constraint solution. 50

6.1 Summary results of the validation studies 72

Chapter 1

Introduction

The development of morphing structures for current aircrafts, especially fixed-wing aircrafts, has become of great interest in the last few years since its design and consequent implementation would allow a great improvement in the performances of such aircrafts. Normally, modern aircrafts design is optimized for only a single point in terms of speed and altitude being their performance out of this point highly improvable. A good example of this can be seen in the slender profiles that are preferable in high velocity regimes and the high curved and thick airfoils that are usually required when taking off and landing. Thus, an aircraft able to adapt itself so as to be always in the optimal point would be of great interest for the aerospace industry since one of the most remarkable advantages of morphing aircrafts is the reduction of fuel consumption.

Achieving just a small percentage of fuel consumption would led us to a great saving in aircraft operational costs. Due to the fact that the amount of fuel that can be stored in an aircraft is limited, this saving would led us to a greater range or endurance in flight. In the medium and long-term period, the capability of an aircraft to adapt itself in order to be always in the optimal configuration seems the only way to achieve more efficiency. When aircraft adaptability is extended to highly significant changes in airplane shape, the word morphing is adopted in place of adaptability.

Aircraft morphing has existed and has been a main driver for designers since the birth of aviation throughout its life. It can be seen from the very primitive wing warping of the Wright Flyier, which used pulling braces to change the configuration of the wing tip to the modern Variable Camber Wing (VCW) concepts, passing through the well known trailing edge flaps, leading edge slats, variable sweep wings, retractable

landing gear or variable pitch propellers.

As it can be seen most of the morphing concepts are focused on the wing, being the main generator of lift. In what follows a concept of an Adaptative Compliant Wing (ACW) composed by a traditional central wingbox with a morphing trailing edge attached to it is proposed. Different configurations have been exploited in order to choose the optimal one not only in terms of better shape change but also in terms of minimum actuation force, when possible, stress levels and feasibility of the solution. This last feature must be always kept in mind since it cannot be forgotten that we hope this concept to be applicable to real wing structures, as a transition between conventional aircraft wings to more futuristic fully-morphing wings.

1.1 Morphing overview

As already said morphing technologies are mostly focused on the wing, since it is the main lift generator. Literature reports several morphing wing concepts that have been demonstrated up to wind tunnel experiments or limited flight tests. In what follows some remarkable contributions are highlighted.

Roth et al [11, 12], using a genetic algorithm to define the optimal wing geometry morphing in flight, demonstrated a potential weight saving of about 8% of take-off gross weight. Spillman [6] showed a potential reduction in drag, mass and direct costs for transport aircraft, arising from the reduction in fuel burn, when variable gapless wing camber are adopted. The University of Bristol, in the framework of Morphing Wing Project [7], emphasized that the potential advantages for applying morphing technologies can be divided into four categories, such as: improve aircraft performance to expand its flight envelope; replace conventional control surfaces for flight control to improve performance and stealth; reduce drag to improve range and reduce vibration or control flutter to improve comfort, safety and reduce fatigue.

Vio et al [8], from University of Liverpool, proposed a different approach, where the aerodynamic forces acting upon the wing are used to provide the moment to twist the wing. By changing the position of the shear centre of the wing, modifying the internal structure, the torsion moment, and hence the amount of twist, will also change. The key idea is that a far smaller amount of energy is required to adjust the structure compared to that required to twist the wing and keep it in that shape.

Focusing on one of the most promising and investigated morphing concepts, such

as the variable wing camber, it is worth remembering some pioneering activities performed in US. At the end of '80 the US Air Force Research Laboratory at Wright-Patterson started a program called Mission Adaptive Wing (MAW), where a F-111 aircraft was equipped with a quite complicated actuation system to smoothly change the wing airfoil during the flight. Late '90s the Active Flexible Wing (AFW) programme by NASA and Rockwell International coupled flexible wings with multicontrol surfaces techniques for the wing aeroelastic control in a beneficial way. By extending the same concept, the Active Aeroelastic Wing (AAW) research programme led by US Air Force Research Laboratory (AFRL) Wright-Patterson Air Force Base, NASA Dryden Flight Research Center and Boeing Phantom Works started in the mid-1990s used wing flexibility as a benefit to increase control power, reduce drag, manoeuvre loads and mass, and enlarge the design envelope. The concept was demonstrated by an extended flight test campaign on a modified F/A-18 with new wing panels made of thinner composite skins with a honeycomb substructure [9, 10]. Monner, at the DLR (German Aerospace Centre), investigated a variable camber wing with flexible trailing edges where the ribs are composed by different elements connected together by hinges and the skin glides over the ribs [15].

The next generation of these morphing devices leads to the definition of wings based on the concept of adaptive structure. In many cases these new structural concepts are strictly related to the currently available technologies. Recent developments in actuation and sensing technology have restored energy in the research of adaptive aircraft structures. Smart material based technology may be applicable to the design of adaptive structures, thus reducing the complexity due to mechanical hinges and numerous moving parts by means of embedded and distributed actuation devices. The synthesis of smart structures can be accomplished by attaching actuators and sensors to conventional structures or by synthesizing composite systems containing several active constituents and using these new materials to build the structures [16]. Smart actuators and materials can be shape memory alloys (SMAs) and lead zirconate titanate (PZT) and they can provide light-weight actuation devices, but their scalability is uncertain when realistic scale problem are considered. An alternative approach is to focus on the structure [17]. In order to obtain new structural concepts able to meet all aeronautical requirements in addition to the required shape change, the synthesis of compliant mechanisms by efficiently distributing the elastic energy into the optimized structure by means of few actuators, can be investigated. This approach is based on

an extension of the distributed compliance concept, originally proposed by Kota [18], instead of the distributed actuation one and leads to compliant structures.

Following this idea, it is worth noting the research on morphing wings at Dipartimento di Ingegneria Aerospaziale - Politecnico di Milano (DIA-PoliMi) focused on two main directions: first, the development of advanced tools for aircraft conceptual design, able to fully include aeroelastic analysis and optimization capabilities even in presence of morphing devices [1]; then, the development of specialized tools for the design of morphing wing able to support the designer in the definition of the wing configuration. Main pillar of this design tool is an alternative approach to obtain the required shape change using few actuators by efficiently distributing the elastic energy into the optimized structure. The proposed approach is built-up on the basis of previous experiences in the design and implementation of the Active Adaptive Wing Camber (AAWC) concept [18, 19], the mechanism developed by DIA-PoliMi for the active camber concept implementation based on a modification of the original idea proposed by Monner from DLR and called for sake of simplicity Rotating Ribs (RR) concept. The comparison between the DIA-PoliMi implementation of the AAWC concept and the ACW wing, equipped with the morphing trailing edge flap proposed in this master thesis, is shown in Figure 1.1.

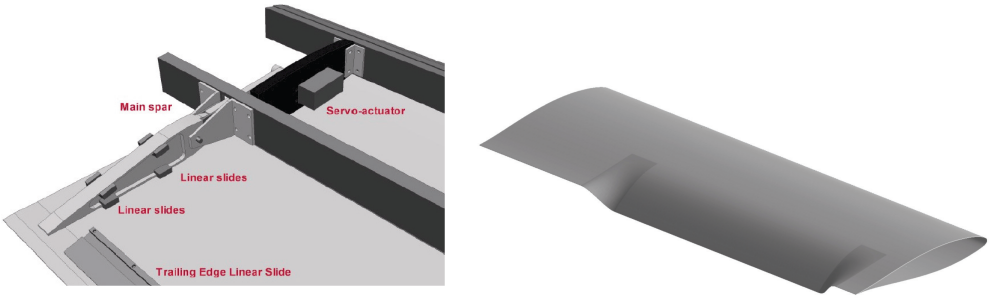

Figure 1.1: DIA-PoliMi rotative rib mechanism (left) and an adaptive compliant wing trailing edge flap (right).

1.2 Objectives

This work presents the process of the design of a morphing trailing edge based on a compliant structure by means of a topological optimization. The optimization is performed thanks to a previous work based on a genetic optimizer [2]. The main objective

of this master thesis is to proof the effectiveness of the design of a compliant morphing trailing edge for a real medium range aircraft wing coming from SARISTU European project.

Such effectiveness will not only be measured in terms of proximity of the deformed wing to the target shape but also in terms of stress levels, actuation forces and feasibility of the potential real structure. To this aim different configurations of morphing trailing edge have been explored.

It will be demonstrated as well, how by performing multiobjective studies structural requirements representing the load-carrying capabilities of the compliant mechanism can be satisfied. The compliance of the solutions will be examined in a final 3D validation study.

1.3 Outline

The work that is here presented is structured in seven chapters. After the first introductory chapter, **chapter 2** states some theoretical aspects about the multiobjective optimization applied to compliant mechanism. To this end, it is also explained the load path representation used for the compliant structure based on previous works highlighting the design variables and how the optimization problem is set. After that, a review of Elitist Non-Dominated Sorting Genetic Algorithm is introduced, since this has been the multiobjective optimization approach adopted for the multiobjectives studies.

In **chapter 3** it is presented an overview of SARISTU FP7 project in which it is justified the origin of the reference wing whose optimization is the main aim of this work.

In **chapter 4** it is reported the procedure adopted by Politecnico di Milano for representing the airfoil shapes both the undeformed configuration and the morphing one, the so called PHORMA (Parametrical sHapes for aerOdinamic and stRuctural Modelling of Aircrafts). After that, it will be explained how from the CAD of the reference wing the morphing shapes have been obtained reporting the different configurations and load conditions for the trailing and leading edges, although only the first one is the objective of these studies.

Chapter 5 deals with the proper optimization procedure presenting the results achieved throughout the studies. Different configurations will be exploited and critically presented. After carrying out the preliminary studies considering just the kine-

matic objective represented by the LSE (Least Square Error) a structural requirement will be added in order to perform the multiobjective studies. This structural requirement represents the load-carrying capability of the structure.

Finally, the validation study of the 3D reference wing is performed in **chapter 6**. To this end, an extension of the solutions found in the previous chapter is performed. After doing so, different actuation performances will be considered in order to appreciate the compliance of the structure.

Possible future studies and developments together with conclusions are given in **chapter 7**.

Chapter 2

Multiobjective optimization of compliant mechanism using Genetic Algorithms

This chapter, in first place, presents the load path representation approached used in this work for the synthesis of compliant mechanism. Secondly an overview of the Non-Dominated Sorting Genetic Algorithm (NSGA-II) used in the hereafter presented multiobjective studies is reported. For the sake of simplicity, and since that is not the main objective of this master thesis, mathematical developments are not included.

2.1 Load path representation

The load path representation is a unified approach for the synthesis of compliant mechanisms based on a design parametrization method employing both discrete (topology) and continuous (size) variables.

In the cases concerning us there are three classes of essential points: input, output, and fixed points (ground supports), but the second one includes a set of so-called active output points placed along the structure boundary. The essential points are always connected directly or indirectly to each other to form a connected structure. According to the theory of topology optimization [2], the load path representation is a design domain parametrization using the load paths to represent different topologies and beam cross sectional areas for size optimizations. In addition to the design variables, also

fixed parameters are included into the load path representation.

2.1.1 Design variables

When the load path representation is applied to shape control problems, the design variables include path sequence (*Seq*), binary path existence variable (*Top*), internal connection point locations (*InterLoc*) and cross sectional load path sizes (*Dim*). As far as shape control problems are concerned, in the design variables must be included as well the load path output destination (*Dest*) and structure boundary size (*hBound*). The initial values of *Seq*, *InterLoc* and *Dest* must be provided by the designer through a Graphical User Interface, but the others instead are randomly generated when the initial population of the genetic algorithm is created.

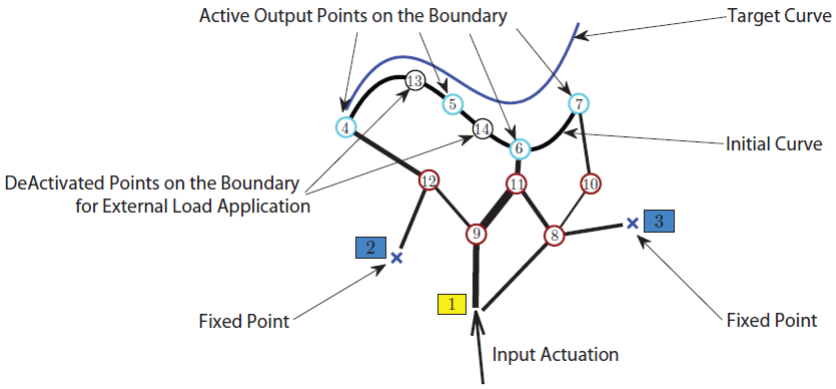

Figure 2.1: A demonstrative connected load path representation of a SIMO compliant mechanism and the corresponding four types of characteristic points: active output points (cyan), deactivated output points (black) for the external load application, internal structure points (red), input actuation point (yellow) and constraint points (blue).

The definition of Seq variable is based on the connections between the essential points. There are three types of characteristic points defining the load paths: input and output active points (*InOut* paths), input and constraint points (*InSpc* paths) and constraint points and active output points (*SpcOut* paths). In Figure 2.1 it can be seen a SIMO compliant mechanism. In addition to this essential points, another class of vertices (8-12 in Figure 2.1) are introduced to allow intermediate connections between different paths: they are the structure internal points. As it will be later on explained, these internal points, although provided by the designer, can move within the design

domain during the optimization procedure.

A binary topology variable *Top* is then assigned to each path in the graph to indicate the presence or absence of the path. When all the *Top* values are 1 in a design, the topology graph is called fully connected; when some of the *Top* are switched to 0, the associated load paths are turned off in the graph, thus creating a partially connected graph that represents a different topology. The binary variable represents the presence of an entire load path, rather than just an element as in a discrete ground structure parametrization. Thus, structural connectivity can be ensured by monitoring the *Top* values in each type of path. The final topology is a union of all the load paths described by *Seq* and *Top*. Genetic Algorithm starts with a group of generated designs in the initial population where the path sequences are interactively determined by the designer, while the corresponding set of binary variables values is randomly generated. Thus various topologies can be explored simultaneously in the synthesis process as the population evolves.

Within the variable *Seq*, the last connection is an integer design variable, called *Dest*. Changing its value the active output point, which the specific load path is attached at, changes. In our case, the input load is transferred from the actuator to the point of the skin. These integer values are randomly assigned in the initial population and correspond to the identification number of the active output points. Points [4, 5, 6, 7] in Figure 2.1.

Unlike the ground structure method, where the final design depends on the initial mesh resolution, load path representation allows variable resolution by varying the locations of the internal points corresponding to the design variable *InterLoc*: all the internal points can move within the design domain. They control the lengths and orientations of the segments in the graph, hence the shape of the compliant mechanism. These internal points must me located either by means of a Graphical User Interface or by specifying their coordinates manually by the designer before defining the load paths that are to be included in the initial population.

For each path in the load path representation, a size array variable *Dim* is used to describe the load path cross sectional dimensions. It is assumed that every segment in the graph represents a beam element with uniform rectangular cross sectional area. Since each load path consists of several segments, *Dim* contains a sequence of values representing the dimensions of the segment composing the load path.

Also the structure boundary cross sectional dimensions (skin) represent a design

variable, called *hBound*. The value of this variable affects the ability of the structure to deform its external shape. When Genetic Algorithm starts, both *Dim* and *hBound* initial values are randomly determined between lower and upper size bounds imposed by the designer as design parameters.

2.1.2 Parameters

Parameters are constant values that remain the same during the optimization and the designer can choose different parameter values to explore different solution space. Several parameters are used in the load path representation. The first one is the number and the initial positions of internal points. The number of internal points *ninter* determines the maximum number of beams that a path can contain *maxPathLength*, which is equal to $ninter + 1$. Not all internal points are used in every design, the number of internal points only provides an upper bound of the mesh complexity. Generally a set of four to ten internal points are sufficient in order to limit the complexity while allowing internal interconnections. This number has been set to five in this case. As far as the constraint points are concerned, they are specified by the designer. Regarding the output points, the number of such points must be provided by the designer n, although their position is found by optimization, in such a way to reduce the number of design variable and, at the same time, allow the optimal control of every point along the airfoil skins.

Because the shape change can be achieved with minimum error, a piecewise linear function is used to fit the curvature difference function $\Delta\kappa(l)$. A continuous optimization process, coupled with the CST technique, is used to find the optimal locations of the active points, while the optimization constraints avoid the active points overlap each other and they go out of the airfoil skin ends. A Sequential Quadratic Programming (SQP) algorithm is employed and the objective function is defined as the fitting error between the curvature difference function interpolated and computed by the CST (section 4.1) method:

Minimize:

$$(\Delta\kappa_n(l) - \Delta\kappa_{CST}(l))^2 \tag{2.1}$$

such that:

$$l_i - l_{i+1} < 0, i = 1, ..., n-1 \tag{2.2}$$

$$l_{low} \leq l_i \leq l_{up}, i = 1, ..., n \tag{2.3}$$

where $\Delta\kappa_n(l)$ and $\Delta\kappa_{CST}(l)$ are respectively the linear interpolation of the curvature difference function evaluated in the n points corresponding to the optimal active output points and the curvature difference function analytically computed by means of the CST technique as described in section 4.1.2; l is the airfoil arc length and (l_{low}, l_{up}) are the corresponding lower and upper bounds at the ends of the the airfoil skins. An example can be seen in Figure 2.2.

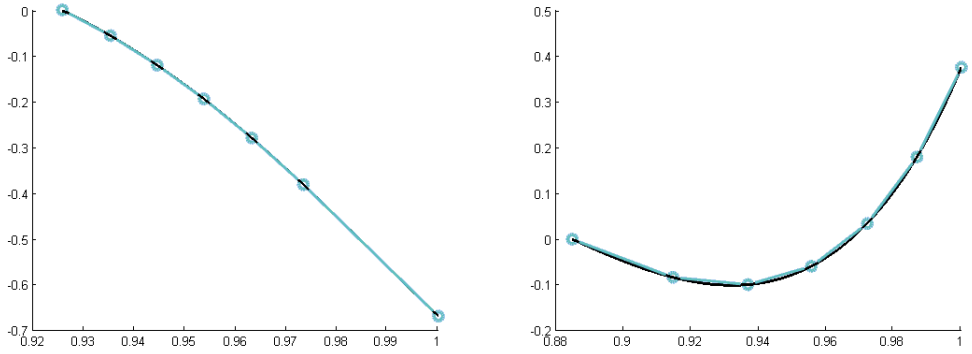

Figure 2.2: Optimal active points location for upper skin of inboard (left) and outboard (right) regions.

Other parameters also include the material Young's modulus for both the load paths and skin (E), maximum and minimum in-plane beam and structure boundary dimensions (*Dim* and *hBound*), and all parameters associated with the genetic algorithm.

2.1.3 Number of design variables

Since the locations of the internal points can vary continuously inside the design domain, variable structure resolution can be considered and a variety of configurations can be investigated without increasing the number of design variables. In order to facilitate the search of the simplest designs which meet the design requirements, a load

path can connect an essential point to every other essential point of a different class. For this reason, the total number of load paths for each design can be uniquely determined by the number of points in each class and all designs can be described by the same number of load paths for the same problem. Once the number of active output points $nout$, actuator input points nin, structure constraint points $nspc$ are known, the number of corresponding load paths can be defined as follows: $ninout = nin \cdot nout$; $ninspc = nin \cdot nspc$; $nspcout = nspc \cdot nout$. The sum $np = ninout + ninspc + nspcout$ represents the maximum number of load paths of each design. The total number of design variables, corresponding to the length of the chromosome array, is:

$$nvar = nSeq + nDest + nBin + nDim + nhBound + nInterLoc \tag{2.4}$$

where $nSeq = np$ is the number of path sequence variables, $nDest = ninout + nspcout$ the number of path destination variables, $nBin = np$ the number of binary path existence variables, $nDim = np \cdot maxPathLength$ the number of path cross sectional dimension variables, $nhBound$ the number of boundary dimension variables, $nInterLoc = 2 \cdot ninter$ the number of internal point coordinates for 2D problems.

2.1.4 Finite Volume Beam models

The beam model for a design can be generated by replacing the vertices and segments of the graph with nodes and Finite Volume beam elements [13, 14]. The nodes are created based on the locations of the essential and internal points, while the element connections can be constructed from the Seq and the element cross sectional dimensions information are contained in the Dim variables.

In order to calculate the deformed curve every set of load path is transformed into a corresponding structural model where each load path is translated into a sequence of Finite Volume Beam connections. When two load paths have overlapping segments, the two corresponding beam elements and their cross sectional dimensions are combined. Moreover, following the idea proposed in [24], new structural grid points are introduce where two beam element cross each other. Since the use of non-linear analysis can be fundamental to describe the behavior of mechanisms subject to large displacements, like in SISO problems, the equilibrium equation is represented by the residual convergence $r = 0$. This is one of the optimization constraints included in the problem formulation.

2.2 Multiobjective optimization using Genetic Algorithms

Most real world optimization problems usually involve multiple objectives, where different solutions may produce trade-offs among them. A solution that is optimal with respect to one objective requires a compromise in other objectives. On the other hand, Genetic Algorithms can find multiple optimal solutions in one single simulation run due to their population-approach. Thus, they are ideal candidates for solving multiobjective optimization problems.

The approach hereafter used for solving this kind of problems applied to our purposes is the so called Elitist Non-Dominated Sorting Genetic Algorithm (NSGA-II). Like in other Genetic Algorithms offspring population Q_t is first created using the parent population P_t, however, in this case, instead of finding the non-dominated front of Q_t only, the two former populations are combined together to form R_t of size $2N$, where N is the population size of P_t and Q_t. Then, a non-dominated sorting is used to classify the entire population R_t. Obviously, this strategy requires more effort compared to performing the non dominating sorting only on Q_t, but it permits a global non-domination check among the offspring and parent solutions. Once this non-dominated sorting is over, the new population is filled by solutions of different non-dominated fronts, one at a time in the following way: the filling starts with the best non-dominated front and continues with solutions of the second non-dominated front, followed by the third non-dominated front, and so on. Due to the fact that R_t is of size $2N$ the fronts that are non accommodated are simply neglected. It may happen that it can exist more solutions in the last allowed front than the remaining slots in the new population as it can be seen in Figure 2.3. Instead of arbitrarily discard some members from the last front, it would be wise to use a niching strategy to choose the members of the last front, which reside in the least crowded region in that front.

The early stages of the evolution are not very much affected by such strategy because in this case many fronts exist in the combined population. Probably, solutions of many good non-dominated fronts are already included in the new population before they add up to N and thus, it hardly matters which solution is considered to fill the population. However, during the latter stages of the evolution, it is likely to happen that most solutions in the population lie in the best non-dominated front. In addition, it may occur that in the combined population R_t, the number of solutions in the first non-dominated front exceeds N. This algorithm ensures that niching will choose a diverse set of solutions from this set. When the entire population converges to the

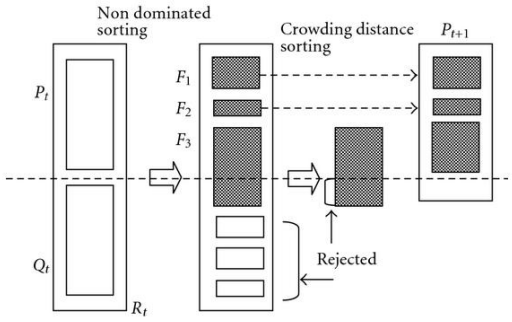

Figure 2.3: NSGA-II procedure.

Pareto-optimal front, the continuation of this algorithm will ensure a better spread among the solutions.

In which follows, the steps of the algorithm are listed. Initially, a random population P_0 is created. The population is sorted into different non-domination levels. Each solution is assigned a fitness equal to its non-domination level (1 is the best level). Binary tournament selection, recombination and mutation operators are used to create an offspring population Q_0 of size N.

- Step 1: Combine parent and offspring populations and create $R_t = P_t \cup Q_t$. Perform a non-dominated sorting to R_t and identify different fronts: $\mathcal{F}_i$, $i = 1, 2, .., etc$.
- Step 2: Set new population $P_{t+1} = 0$. Set a counter $i = 1$. Until $|P_{t+1}| \, | \, |\mathcal{F}_i| < N$, perform $P_{t+1} = P_{t+1} \cup \mathcal{F}_i$ and $i = i + 1$.
- Step 3: Perform the crowding-sort ($\mathcal{F}_{i,} <_c$) procedure and include the most widely spread ($N - |P_{t+1}|$) solutions by using the crowding distance values in the sorted $\mathcal{F}_i$ to P_{t+1}.
- Step 4: Create offspring population Q_{t+1} from P_{t+1} by using the crowded tournament selection, crossover and mutation operators.

In Step 3, the crowding-sorting of the solutions of front *i* (the last front which could not be fully accommodated) is performed by using a *crowding distance metric*. The population is arranged in descending order of magnitude of the crowding distance values. In Step 4, a *crowding tournament selection operator*, which at the same time uses the crowding distance, is used.

It is worth noting that the non-dominated sorting in Step 1 and filling up population P_{t+1} can be performed at the same time. Doing so, whenever a non-dominated front shall be found, its size can be used to check if it can be included in the new population. If this is not possible, no more sorting is required. This fact helps in reducing the simulation run time.

The already mentioned *crowding tournament selection operator* consists of: A solution i wins a tournament with another solution j if any of the following conditions are true:

1. If solution i has a better rank, that is, $r_i < r_j$.
2. If they have the same rank but the solution i has a better crowding distance than solution j, that is, $r_i = r_j$ and $d_i > d_j$.

The first condition ensures that the chosen solution lies on a better non-dominated front. The second one resolves the tie of both solutions being on the same non-dominated front by deciding on their crowded distance, in such a way that the one residing in a less crowded area wins.

Regarding the crowding distance, it is an estimate of the density of solutions surrounding a particular solution i in the population. We take the average distance to two solutions of either side of solution i along each of the objectives. This distance d_i gives an estimate of the perimeter of the cuboid formed by using the nearest neighbors as the vertices as can be noticed in Figure 2.4 in which the crowding distance is the average side-length of the cuboid.

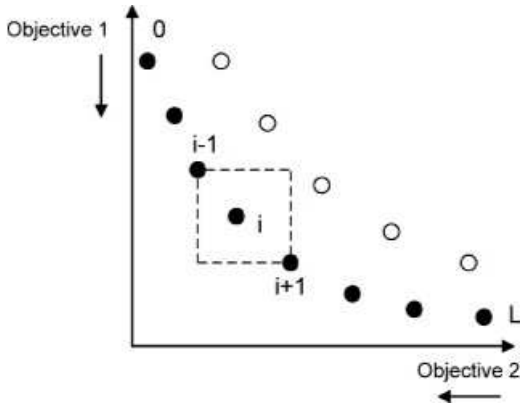

Figure 2.4: Crowding distance calculation.

In what follows the *crowding distance assignment* procedure ($\mathcal{F} <_c$) is shown:

- Step C1: Call the number of solutions $\mathcal{F}$ as $l = |\mathcal{F}|$. For each i in the set, first assign $d_i = 0$.
- Step C2: For each objective function $m = 1, 2, ..., M$, sort the set in worse order of f_m or, find the sorted indices vector: $I^m = sort(f_m, >)$.
- Step C3: For $m = 1, 2, ..., M$, assign a large distance to the boundary solutions, or $d_{I_1^n} = d_{I_1^m} = \infty$, and for all other solution $j = 2$ to $(l - 1)$ assign:

$$d_{I_i^n} = d_{I_i^m} + \frac{f_m^{(I_{j+1}^m)} - f_m^{(I_{j-1}^m)}}{f_m^{max} - f_m^{min}} \tag{2.5}$$

The index I_j denotes the solution index of the $j - th$ member of the sorted list, and thus, for any objective, I_1 and I_l denote the lowest and highest objective function values, respectively. The second term of the right side of Equation 2.5 represents the difference in objective function values between two neighboring solutions on either side on I_j. Then, this metric represents half the perimeter of the enclosing cuboid with the nearest neighboring solutions placed on the vertices of the cuboid (Figure 2.4). It is worth noting that for any solution i the same two solutions $(i + 1)$ and $(i - 1)$ do not need to be neighbors in all the objectives, in particular for $M \geq 3$. The parameters f_m^{max} and f_m^{min} can be set as the population-maximum and population-minimum values of $m - th$ objective function.

The above metric requires M sorting calculations in Step C2, each requiring $O(N \log N)$ computations. Step C3 requires N computations, thus the complexity of the above distance metric computation is $O(MN \log N)$. For large N, this complexity required is smaller than $O(MN^2)$, which denotes the computational complexity required in other niching methods.

Since solutions compete with their crowding distance, no extra niching parameter is needed here. The elitism mechanism does not allow an already found Pareto-optimal solution to be deleted. However, when the crowded comparison is used to restrict the population size, the algorithm losses its convergence property. As long as the size of the first non-dominated set is not larger than the population size, this algorithm preserves all of them. Nevertheless, in latter generations, when more than N members belong to the first non-dominated set in the combined parent-offspring population, some closely-packed Pareto-optimal solutions may give their place to other non-dominated yet non-Pareto-optimal solutions. Although these latter solutions may get dominated by other Pareto-optimal solutions in a later generation, the algorithm can resort into

this cycle of generating Pareto-optimal and non-Pareto-optimal solution before finally converging to a well distributed set of Pareto-optimal solutions.

As already mentioned, the non-dominated sorting needs to be performed on a population of size $2N$, instead of a population of size N required in most algorithms.

Chapter 3

Reference wing

This chapter makes reference to the origin of the reference wing whose trailing edge will be optimized hereafter. This work is held in the framework of an European project called SARISTU FP7 led by Airbus in which 64 partners from 16 countries participate. After so, the CAD of the reference wing from which both the undeformed and the morphing shapes have been extracted will be presented.

3.1 SARISTU FP7 project

SARISTU (Smart Intelligent Aircraft Structures) is an European project supported by the European Comission (Seventh Framework Program - FP7) and led by Airbus focused on the cost reduction of air travel through a variety of individual applications as well as their combination. For the first time ever in smart material concepts, this project offers the opportunity to virtually and physically assess the interaction of different technological solutions and their combined effects at aircraft level. Self-Sensing Structures, Nanotechnologies and Morphing are the three pillars of this new integrated approach for future Smart Airframes to be realized in SARISTU.

Specifically, the joint integration of different conformal morphing concepts in a laminar wing is intended to improve aircraft performance through a 6% drag reduction, with a positive effect on fuel consumption and required take-off fuel load. A side effect will be a decrease of up to 6dB(A) of the airframe generated noise, thus reducing the impact of air traffic noise in the vicinity of airports. Past research has shown the economic feasibility and system maturity of aerodynamic conformal morphing. How-

ever, few projects concerned themselves with the challenges arising from the structural integration on commercial aircraft. In particular, the skin material and its bonding to the substructure are challenging. One of the SARISTU goals is to demonstrate the structural realizability of individual conformal morphing concepts concerning the leading edge and the trailing edge on a full scale outer wing section by aerodynamic and structural testing.

Another important objective is to limit the integration cost of Structural Health Monitoring (SHM) systems by moving the system integration as far forward in the manufacturing chain as possible. In this manner, SHM integration becomes a feasible concept to enable in-service inspection cost reductions of up to 1%.

Operational requirements on conformal morphing surfaces necessitate the implementation of an independent, integrated shape sensing system to ensure not only optimal control of the aerodynamic surface but also failure tolerance and robustness. Developments made for structural health monitoring will be adapted to this task. Similar systems optimized for rapid in-service damage assessment have progressed to a maturity which allows their inclusion in the next generation of aircraft. However, the time consuming application of these sensor systems has to be further improved by integration at the component manufacturing level. The additional benefit of a utilization of these adapted systems for part manufacture process and quality control shall be assessed in SARISTU.

Finally, the incorporation of Carbon Nanotubes into aeronautical resins is expected to enable weight savings of up to 3% when compared to the unmodified system of skin, stringer and frame, while a combination of technologies is expected to decrease Electrical Structure Network installation costs by up to 15%.

SARISTU Consorptium brings together 64 partners of 16 European countries, Politecnico di Milano among them. The structure of the activities of SARISTU European project are summarize in Figure 3.1.

3.2 Reference wing CAD

The process hereafter described was applied to the SARISTU wing in order to analyze different morphing configurations, such as those shown in Figure 3.2. Different sections were identified in order to reproduce the correct reference shape and to have a wing mathematical model suitable to be used to introduce the shape changes into the

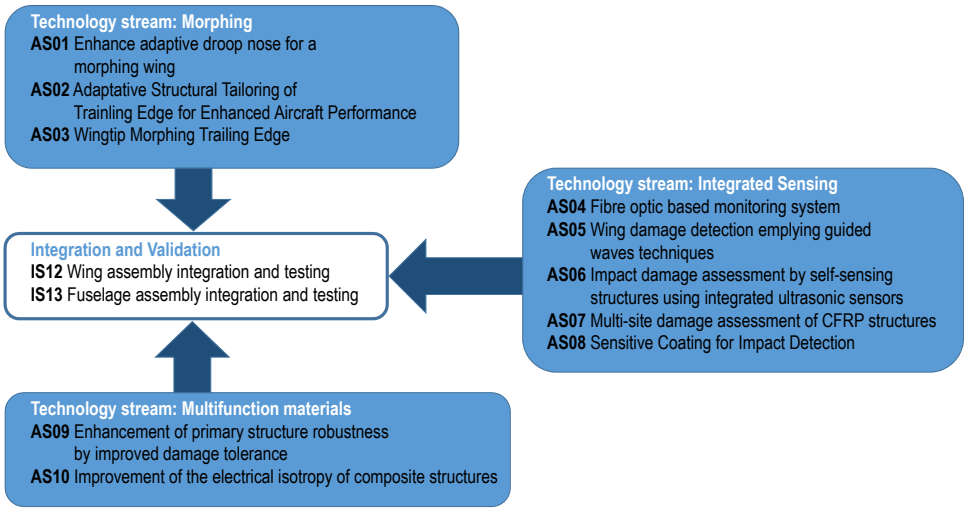

Figure 3.1: Structure of the activities taking place in the SARISTU project.

trailing and leading edge morphing devices.

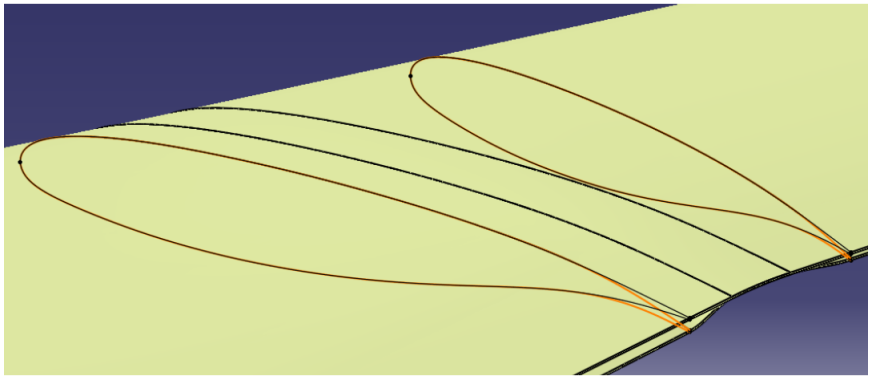

Figure 3.2: Morphing configuration of SARISTU reference wing CAD.

One of the problems in analyzing different morphing concepts is related to the need to create in an efficient way all the necessary morphing geometry models representing the morphing devices in their different status, taking into account structural and aero-

dynamic requirements. The approach adopted by POLIMI is based on a procedure developed in a previous work [4, 5], tuned for specific morphing devices. The generation of the geometry model of the 3D full wing corresponding to the different position of the morphing devices is based on the use of PHORMA and it is done in three steps, as shown in Figure 3.3: a 2D identification of the initial airfoils, a morphing shape optimization able to introduce the shape changes under all the design requirements and a 3D extension to the full wing. The core of the 2D identification process is based on the hereafter described CST method. Starting from a 3D CAD model, a set of airfoil shapes is extracted and locally identified in a parametric way together with a set of attributes including the position and the orientation of corresponding sections. After that the airfoil shapes can be modified by means of the morphing shape optimization and combined again to build the 3D geometry corresponding to the morphing configuration. Local shape changes can be spread along the wing in span-wise direction via piece-wise linear or cubic interpolation surfaces. The 3D shape coming out from this process can be exported to automatically generate different kind of meshes for aerodynamic or structural computations.

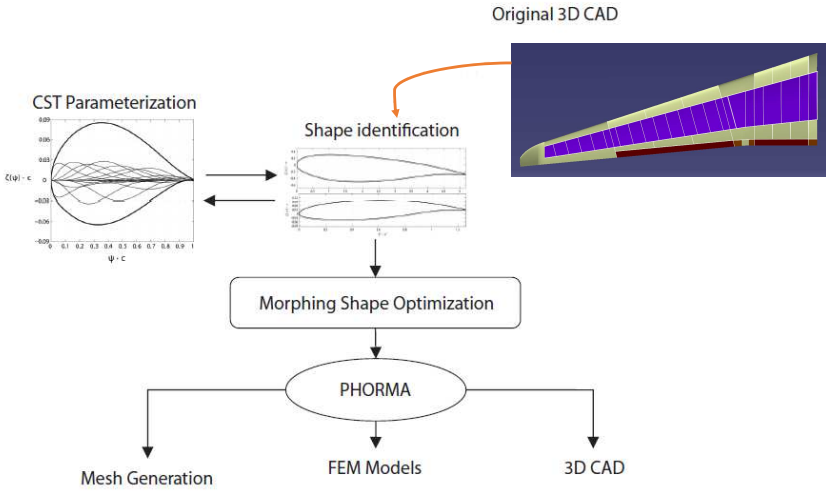

Figure 3.3: Procedure for the generation of morphing models.

Chapter 4

Morphing shapes and aerodynamic loads

In this chapter it is, in first place, described the tool used to represent the airfoil shapes both the undeformed configuration and the morphing one, the so called PHORMA. PHORMA is based on a parametrization technique named Class/Shape function Transformation (CST) that allows the deformation of the global shape of the aircraft without affecting the local regularity of them. Indeed, this tool can be interfaced with CAD models in order to identify some certain section and produce the CFD of FEM mesh for further computations.

After doing so, we will focus on the SARISTU reference wing from which we have extracted the profiles to be optimized. Morphing configurations and a set of 13 Load Cases are reported for both leading and trailing edge, however, the study of the trailing edge will be the main issue of this work.

4.1 Airfoil shape representation (PHORMA)

The procedure adopted by PoliMi for the generation of aerodynamic, structural and CAD aeronautical models is based on the use of a framework called PHORMA (Parametrical sHapes for aerOdinamic and stRuctural Modelling of Aircrafts) [22]. PHORMA is an Object Oriented code composed by a suite of tools that allow to exchange and handle different shapes in order to generate corresponding 3D geometries. These shapes can be provided in discrete, polynomial, spline, CAD-based and analytical form. Start-

ing from a CAD model, the shapes, corresponding to a set of the most important sections of the aircraft model, are locally identified and associated to a set of attributes including the position and the orientation of each shape. These shapes are combined in the three dimensional space through a piece-wise linear or cubic interpolation so that local shapes changes can be spread out. The 3D parametrized geometry can be directly used to produce the CFD or FEM mesh of corresponding aerodynamic or structural models, to provide a fast interface to commercial softwares and to call the commonly used solvers. A graphical representation of the PHORMA layout is shown in the flowchart of Figure 4.1.

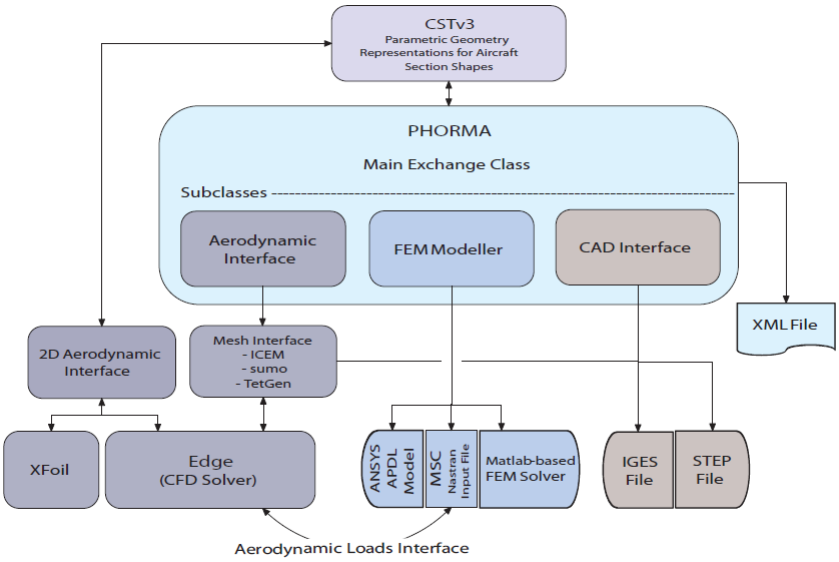

Figure 4.1: The FrameWork PHORMA.

4.1.1 The CST method

The core of PHORMA is a parametrization technique, originally proposed by Kulfan [20, 21] and extended by PoliMi to morphing airfoils [2, 3]. This parametrizations technique is called Class/Shape function Transformation (CST) method and allows to deform the global shape of the aircraft sections without affecting their local regularity. It is based on merging four terms: a Shape Function, a Class Function and two additional terms related to the airfoil leading-edge and trailing-edge shapes. The general mathematical expression representing the airfoil geometry is:

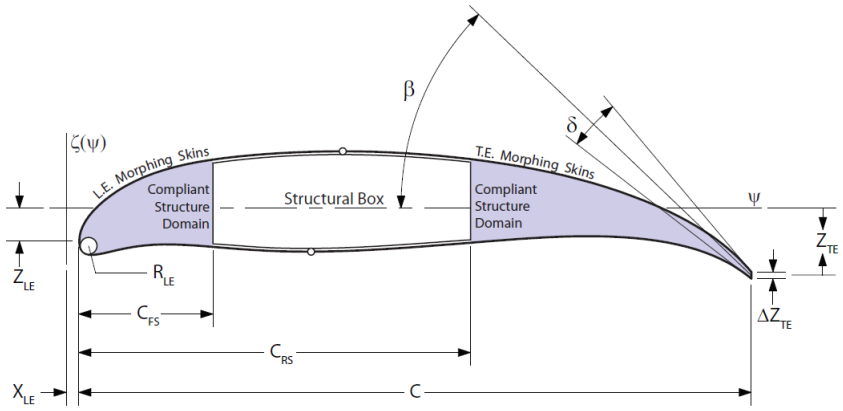

Figure 4.2: The geometric parameters describing the CST approach.

$$\zeta(\psi) = C_{N2}^{N1}(\psi)S(\psi) + \psi\zeta_{TE} + (1-\psi)\zeta_{LE} \tag{4.1}$$

where $\psi = x/c$, $\zeta = z/c$ are the nondimensional coordinates with respect to the airfoil chord c, $\zeta_{TE} = Z_{TE}/c$ and $\zeta_{LE} = Z_{LE}/c$.

The first term of Equation 4.1 is the Class function and provides control of both the leading and the trailing edge shape. Its general mathematical form is defined as follows:

$$C_{N2}^{N1}(\psi) \stackrel{\triangle}{=} \psi^{N1}(1-\psi)^{N2} \tag{4.2}$$

Different combinations of the exponents ($N1$ and $N2$) in the Class function, are used to mathematically define a variety of basic general shapes. In such a ways, round nose, elliptic or minimum drag supersonic biconvex body, as well as rectangle or circular form geometry can be also represented.

The Class function is used to define general classes of airfoil geometries, while the Shape function is used to define specific shapes within the geometry class. The second term of Equation 4.1 is the Shape function of selected order n:

$$S(\psi) = \sum_{i=0}^{n} A_i S_i(\psi) \tag{4.3}$$

The upper and lower surfaces of a general cambered airfoil can be defined using Bernstein polynomials to describe a set of $(n+1)$ component shape functions $S_i(\psi)$

which are scaled by as many unknown coefficients A_i. The component shape functions are defined as follows:

$$S_i(\psi) = K_i \psi^i (1-\psi)^{n-i} \tag{4.4}$$

where $\psi^i(1-\psi)^{n-i}$ represents the Bernstein polynomial and the term K_i is the associated binomial coefficient which is defined as:

$$K_i \equiv \begin{pmatrix} n \\ i \end{pmatrix} \equiv \frac{n!}{i!(n-i)!} \tag{4.5}$$

A series of Bernstein polynomials can be easily extracted from a line of the Pascal's triangle, shown in Figure 4.3. A Bernstein polynomial of a specific order provides a systematic decomposition of the unit shape function into scalable components, over the interval of $0-1$; the individual terms in the polynomial can be scaled to define the approximation of any continuous curve.

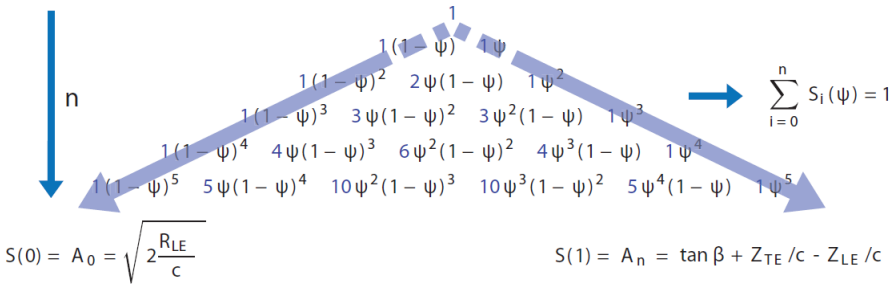

Figure 4.3: The Pascal triangle and the boundary conditions.

In the CST technique, each Bernstein polynomial component is multiplied by the Class function defining the systematic decomposition of the airfoil into the corresponding scalable airfoil components. Consequently, the coefficient A_i multiplies the individual Bernstein polynomial component and can be used to scale the airfoil shape function which is a blended function that eliminates slope or curvature discontinuities. The first and last terms of the shape function are determined by imposing the boundary conditions on the airfoil shape [20]: they are directly related to the airfoil leading edge nose radius R_{LE}, to the trailing edge boat-tail angle β and to the thickness ΔZ_{TE}. These parameters, in addition to the already defined parameter ζ_{TE}, the airfoil

chord c, represent the CST parameters shown in the Figure 4.2. The value of the Shape function at $x/c = 0$ is directly related to the airfoil leading edge nose radius and the airfoil chord length by the following formula:

$$S(0) = A_0 = \sqrt{2\frac{R_{LE}}{c}} \tag{4.6}$$

The shape function value at $x/c = 1$ is related to the airfoil boat-tail β, final trailing edge vertical position Z_{TE} (equal to $\zeta_{TE} + 0.5\Delta Z_{TE}$) and leading-edge vertical position Z_{LE}, by the formula:

$$S(1) = A_n = \tan\beta + Z_{TE}/c - Z_{LE}/c \tag{4.7}$$

The other $n - 1$ terms in the Equation 4.3 neither affect the leading edge radius nor the trailing edge angle and can be used to change the airfoil shape. In this way, the perturbation of one of these coefficients spreads on the entire design space of the airfoil maintaining its local smoothness.

4.1.2 Representation of the morphing airfoil skin structural behavior

The CST parametrization technique is well suited to represent the shape changes of morphing airfoils and it can be also used to describe the structural behavior of the skin. Indeed, thanks to its analytical nature, the calculation of the first and the second order derivatives results very fast and they can be used to compute the length and curvature of airfoil upper and lower surfaces, described by Equation 4.1, as follows:

$$L(x) = \int_0^c \sqrt{1 + \left(\frac{d\zeta}{dx}\right)^2}\, dx \tag{4.8}$$

$$\kappa = \frac{\zeta\mathfrak{t}'\mathfrak{t}'(x)}{(1 + \zeta'^2)^{3/2}} \tag{4.9}$$

While the second one is analytically computed, the first one is evaluated semi-analytically. These geometrical quantities could be strictly related to the structural properties of the morphing airfoil skin. The stress into the skin consist of two terms: the stress due axial tension or compression σ_{axial} and the stress due to bending σ_{bend}. When the airfoil shape changes due to a morphing process, using Equation 4.8, it is easy to compute the length of the both undeformed and morphing airfoil surfaces and

to estimate the axial stress that is required to stretch or compress the airfoil skins. Using Equation 4.9, the bending stress is computed calculating the curvature difference between the initial and the final airfoil shape with respect to the two normalized arc lengths l, as follow:

$$\Delta\kappa(l) = \kappa_m(x(l)) - \kappa_u(x(l)) \tag{4.10}$$

where κ_u and κ_m are the curvature functions of the undeformed and morphing airfoil, $x(l)$ the inverse of normalized are length function that can be computed from Equation 4.8. According to Euler-Bernoulli beam theory, the bending stress along the skin can be calculated from the curvature difference function as:

$$\sigma_{bend} = \frac{Et}{2}(\Delta\kappa(l)) \tag{4.11}$$

where E is the Young's Modulus and t is the skin thickness. Since Equation 4.11 is based on the difference between the final and initial curvature distribution, it is general and suitable to compute stress values due to shape changes corresponding to large displacements. The available length and curvature variations of the airfoil's upper and lower surfaces, strictly related to the axial and bending stresses generated when the skin is forced to assume the morphing airfoil shape, can be used as explicit constraint function to drive the first level optimization procedure.

4.2 Morphing configurations

PHORMA allows to automatically generate 2D structured mesh suitable to perform Navier-Stokes analysis. A sophisticated code was embedded into the CST method to automatically produce the mesh of both clean and morphing airfoils, in order to perform high–fidelity aerodynamic shape optimizations. The details of the completed procedure are shown in Figure 4.4. This high-fidelity feature is to be substituted in the general procedure for the generation of morphing model, described in Figure 3.3.

The first step is to obtain a good parametrization of the reference geometry by means of the tools included in PHORMA. The airfoils geometry is defined by the points extracted from the corresponding reference CAD and the analytical shape describing the same geometry, as calculated from these coordinates, were identified.

The full 3D wing is obtained in a parametrical way by combining a number of

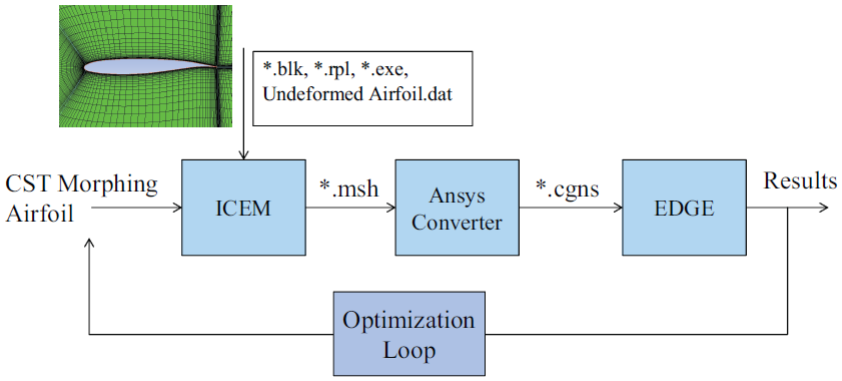

Figure 4.4: Procedure for the generation of morphing models.

airfoil shapes. They were spread along the wing via particular interpolation surfaces able to reproduce the correct wing thickness distribution in span–wise direction, so to accurately describe the original reference wing. Moreover the implemented procedure allows to impose different transition laws of the geometry properties among the different 2D airfoils, as well as to modify their global properties such as angle of attack, dihedral or tow angles. A total of 13 flight conditions have been identified for the reference wing as it can be seen in Table 4.1. The first seven are exactly the same adopted for the aeroelastic design of the wingbox. The other six are more related to the operational conditions of investigated morphing devices. For each flight condition an analysis loop was performed to calculate the angle of attack able to guarantee the value of CL capable of produce the requested lift corresponding to the requested load factor.

Once the parametrical geometry reference wing was generated and validated, it was used to introduce the shape changes into the leading and trailing edge morphing regions. A comparison between the original SARISTU wing geometry and the identified one shows a maximum error of $1.2mm$. Different morphing configurations were studied for both morphing leading and trailing edge. The target shapes the morphing airfoil must assume are derived by a shape optimization problem able to define the best airfoil change to satisfy specifically imposed requirements. One of the most important obstacles in the airfoil morphing is due to the structural contribution of the skin. Since different design requirements can be provided for each morphing device, different shape optimization problems can be tuned. After setting up the optimiza-

tion problem able to meet the design requirements for each specific morphing device, the morphing airfoils, coming out from the optimization process, were combined to produce the 3D geometry model corresponding to the morphing configuration.

3D geometry models corresponding to morphing trailing and leading edge devices were generated. The mathematical advantage of the geometry representation adopted in PHORMA can be evident considering the first derivative, the second derivative and the curvature function. While the airfoil first and second derivatives are infinite at the nose, and the curvature varies greatly over the surface of the airfoil, the first and second derivatives of the Shape function (Equation 4.3) are finite and the curvature of the Shape function is essentially zero. These quantities are important both to determine the accuracy level of the identified geometry models and to estimate the skin structural behavior of the morphing devices.

PHORMA simultaneously allows to mathematically define the morphing wing shape and estimate the stress distribution along the skins and run aerodynamic analysis. This aero-structural scheme allows to combine the estimation of the aerodynamic performances and the skin structural behavior without waiting for the process determines the optimal shape. It is suitable to describe a wide variety of wing shapes using a small number of design variables.

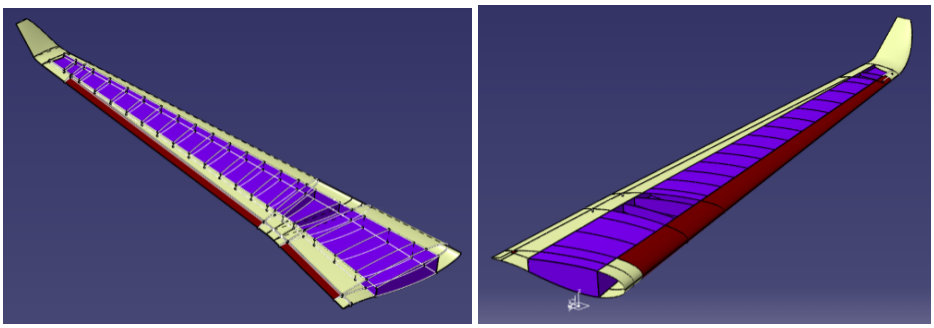

Figure 4.5: SARISTU wing morphing configurations.

4.2.1 Morphing leading edge

The morphing leading edge configuration is full-span and 20% in chord-wise. The main design rule from a structural point of view is keeping the circumferential skin length constant to avoid axial strains. And the amount of droop of the individual

sections depends on the maximum curvature change which is restricted to 20 1/m. The morphing leading edge requirements are:

- Design load condition: Low speed;
- Span: Full span;
- Allowable skin axial strain: 0;
- mTE deflection range: Max value allowed by the curvature constraint;
- Skin bending behavior: maximum curvature change of 20 [1/m] to avoid strains above 1%.

4.2.2 Morphing trailing edge

Concerning the morphing trailing edge, three different configurations were considered:

- Morphing TE along 83% of span and along 10% of MAC.
- Morphing TE along 65% of span (conventional aileron) and along 10% of MAC.
- Morphing TE along 65% of span and along 20% of MAC in the inboard region.

A sub-set of the flight conditions was extracted for the evaluation of high speed morphing devices performances. According to the skin material, a maximum epsilon strain of 2% is allowed. Following requirements were considered:

- Load condition: cruise;
- Chord: 10% or 20% (of the CMA);
- Span: 2 morphing areas in span-wise direction (not tapered segment):
- mTE deflection range: +/- 5%;
- Max skin axial strain: <0.03% (Aluminum alloy) or 4% (SmartMat);

ID	Case	W	Mach	ZFt [kft]	nz (g)	CL	AoA [deg]
Flight conditions for structural box sizing							
1	**Cruise**	MTOW (60 t)	0.484	0	1	0.3223	0.2443
2	**Vc Nz Max**	MTOW (60 t)	0.484	0	2.5	0.8000	5.4961
3	**Vc Nz Min**	MTOW (60 t)	0.484	0	-1	-0.3153	-6.6779
4	**Vd Nz Max**	MTOW (60 t)	0.605	0	2.5	0.5123	1.8400
5	**gust_1**	MTOW (60 t)	0.484	0	3	0.9585	7.4947
6	**STGust (gust_2)**	MLW (55 t)	0.484	0	3.2	0.9261	7.0500
7	**Va Nz Max ***	MTOW (60 t)	0.388	0	2.5	1.2302	13.0000
*Va was computed using the CLmax obtained from the aerodynamic analysis performed on the reference wing							
Flight conditions for morphing device performances evaluation							
8	**Cruise MTOW**	MTOW (60 t)	0.750	35	1	0.5685	1.2700
9	**Cruise MLW**	MLW (55 t)	0.750	35	1	0.5216	0.9214
10	**Climb 0k**	MTOW (60 t)	0.400	0	1	0.4702	2.0406
11	**Climb 20k**	MTOW (60 t)	0.600	20	1	0.4552	1.2935
12	**Climb 30k**	MTOW (60 t)	0.700	30	1	0.5173	1.3357
13	**Low Speed V Max****	MTOW (60 t)	0.250	0	1	1.1972	11.2926
**no Flaps							
14	**Low Speed V Min*****	36 t	0.121	0	1		18.000
***Flaps-no Slat							

Table 4.1: Flight conditions given by Alenia.

4.3 Load conditions

The flight conditions for the reference wing to be analyzed were provided by Alenia and are summarized in Table 4.1:

As far as the trailing edge is concerned the load cases to be considered are cases 1, 8 and 9. Some CFD studies using EULER computation are here reported (see Figure 4.6) on the C_P and Mach distribution along the profiles. In Figure 4.7 we can see a comparison of the polar curves of the 3 morphing configurations so as to appreciate the improvement in the aerodynamic performances. In cruise condition the configuration number 2 gives the greatest benefits and so, it is the one considered in these studies. It should be pointed out that these results are related to the wing and that the benefits would be lower if the contribution of the fuselage was taken into account.

In the following studies load case 1 will be considered for the optimization of the compliant mechanism for the trailing edge of the SARISTU reference wing because

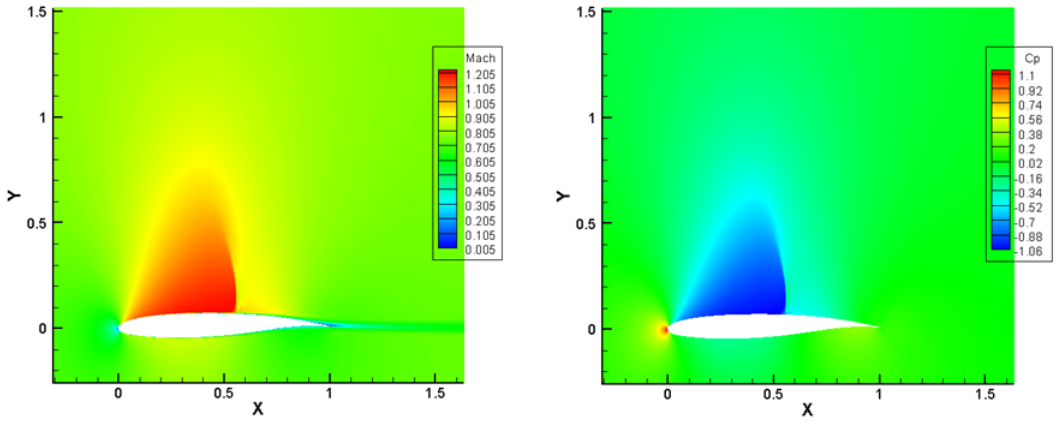

Figure 4.6: Aerodynamic studies of the reference wing for the trailing edge configuration.

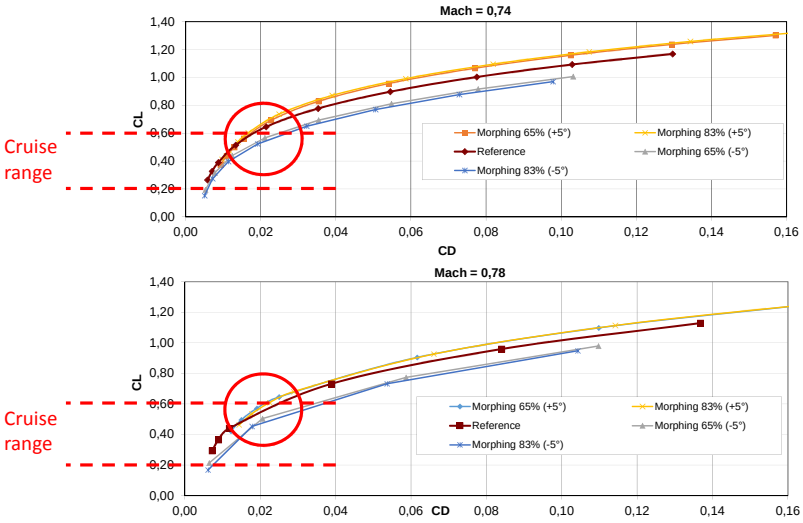

Figure 4.7: Polar curves for the reference wing in the three trailing edge morphing configurations.

of availability issues of the morphing shapes and the fact that among the cruise load cases, that one is the most demanding case. As far as the aerodynamic loads evaluation is concerned, in order to have them in the structural mesh to be used afterward in the optimization procedure of the compliant structure, XFOIL Software for 2D airfoils was used. So as to check the results coming from these analysis, they were compared to EULER computations performed in the 3D reference wing. In Figure 4.8, it can be seen the comparison of the pressure coefficient for a generic section of such wing. It can be perceived that, although the results does not coincide for the leading edge, for the trailing edge, that is the region of interest in this work, they do. This has made XFOIL computation suitable for our purposes.

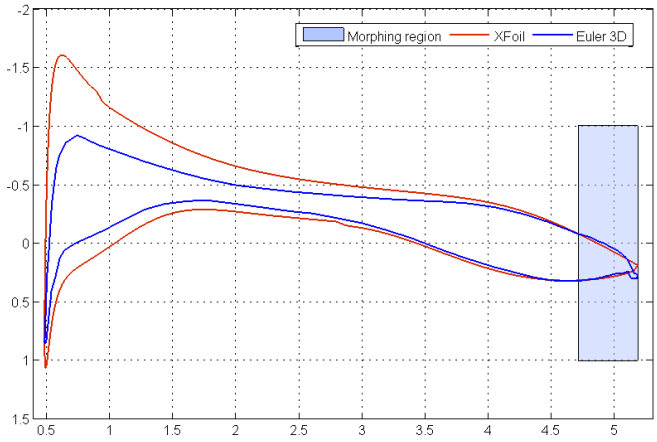

Figure 4.8: C_P comparison between EULER and XFOIL computations.

Chapter 5

Synthesis of morphing airfoils

In this chapter it is performed the proper optimization of the compliant mechanism for the morphing trailing edge of the reference SARISTU wing. First of all, the setup of the optimization problem is given for a SIMO system with only one objective function, which is the Least Square Error between the deformed trailing edge and the target curve.

After that, a single objective optimization is led, testing different configurations of constraints or different materials for skin and load paths. After doing such study, the solutions are refined making use of a multiobjective optimization approach. A structural requirement representing the minimization of the strain energy under the cruise loads is added, and eventually a third objective representing the minimization of the maximum stress is reached.

5.1 Optimization problem formulation

Unlike typical Single-Input Single-Output (SISO) compliant mechanisms, the shape control problem has a Multiple Output (SIMO) nature. As a consequence, a number of points placed along the structure boundary, greater or equal to the number of active output points $nout$, is used to minimize the Least Square Error (LSE) between the deformed curve and the target curve.

The optimization problem tries to minimize the Least Square Error subject to size constraints for the load path beam elements (Dim_{min} and Dim_{max}) and structure boundary elements ($hBound_{min}$ and $hBound_{max}$), the internal point boundaries ((x_{low}, y_{low},

z_{low}) and (x_{up}, y_{up}, z_{up})), two global connectivity equations, stress and buckling constraints ($\sigma_{allowable}$), and the elastic equilibrium equation.

Minimize:

$$LSE = \frac{1}{n}\sum_{i=1}^{n}\sqrt{(x_{d,i} - x_{m,i})^2 + (y_{d,i} - y_{m,i})^2 + (z_{d,i} - z_{m,i})^2} \tag{5.1}$$

such that:

$$Dim_{min} \leq Dim_{i,j} \leq Dim_{max} \tag{5.2}$$

$$hBound_{min} \leq hBound_k \leq hBound_{max} \tag{5.3}$$

$$(x_{low}, y_{low}, z_{low}) \leq interCoord \leq (x_{up}, y_{up}, z_{up}) \tag{5.4}$$

$$\sum_{i \in InOut} Top_i \geq 1 \tag{5.5}$$

$$\sum_{i \in InSpc \cup pathSpcPut} Top_i \geq 1 \tag{5.6}$$

$$\sigma \leq \sigma_{allowable} \tag{5.7}$$

$$r = 0 \tag{5.8}$$

where n is the number of control points placed along the boundary, (x_d, y_d, z_d) are the grid positions in the deformed condition computed by the structural analysis and (x_m, y_m, z_m) the corresponding target shape points. *interCoord* is the coordinates of the internal points, while $Dim_{i,j}$ represents the cross sectional thickness of the $j-th$ beam of the $i-th$ load path and $hBound_k$ the thickness of the k–th structure boundary. The dimension of an element is subject to the constraint of minimum manufacturable feature size.

In the load path representation, the structural topology is described in terms of the presence or absence of individual load paths, thus connectivity information are readily available. The structural connectivity can be ensured by imposing constraints on *Top*.

Top_i represents the binary design variable which determines the presence or absence of the $i-th$ load path and the third and fourth constraints respectively guarantee the global connectivity between input actuator and structure boundary and between the internal structure and structure constraints.

5.2 Preliminary studies

The first step in the optimization of the trailing edge of the wing of interest has been to identify two regions, inboard and outboard, and focus on the design of one reference section for each one, with expectations of extending the solution to the rest of the compliant ribs. The reference sections have been highlighted in Figure 5.1.

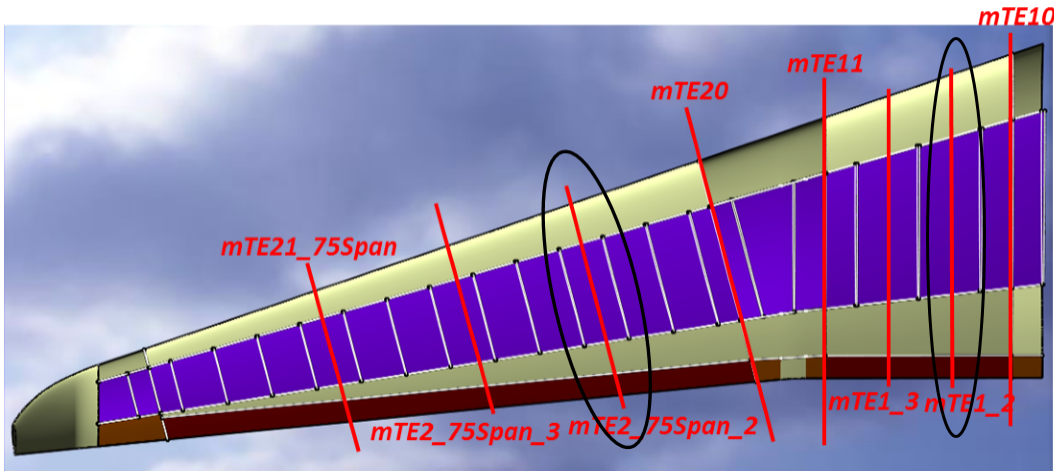

Figure 5.1: Selection of the sections of the reference SARISTU wing to be optimized.

In which follows, the results obtained in the single objective 2D optimization are shown. In general terms the genetic optimizer has started with an initial population of 400 individuals, a crossover fraction of 0.6, and two elite individuals; although in some cases these parameters have been changed so as to better appreciate their effects. The number of load paths corresponding to the initial population has been set to a number around 50. An example of this can be seen in Figure 5.2.

In spite of only little deflection required to be achieved as it can be eminent from Figure 5.3, the optimization is not as trivial as it could be thought, due to the fact that aerodynamic loads for the cruise condition selected are anyways high, as we can see in Figure 5.4, and that there is little space for the compliant mechanism.

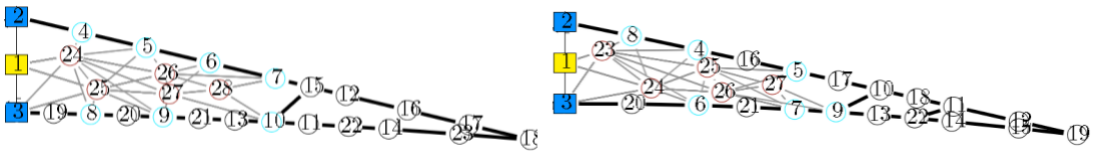

Figure 5.2: Example of load paths corresponding to the initial population.

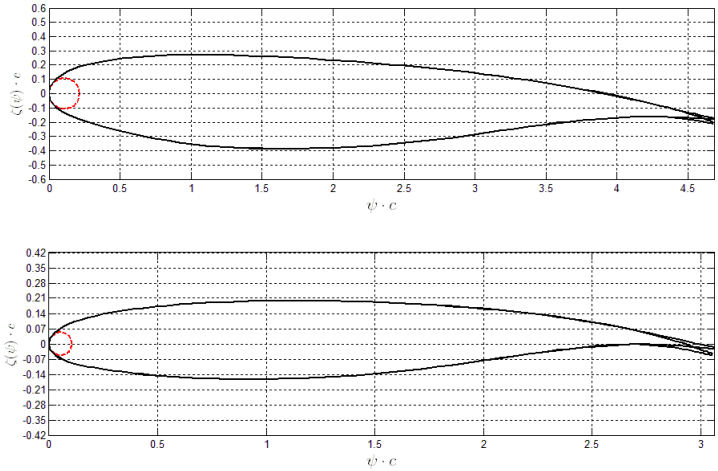

Figure 5.3: Shape change in the reference sections represented as CST objects.

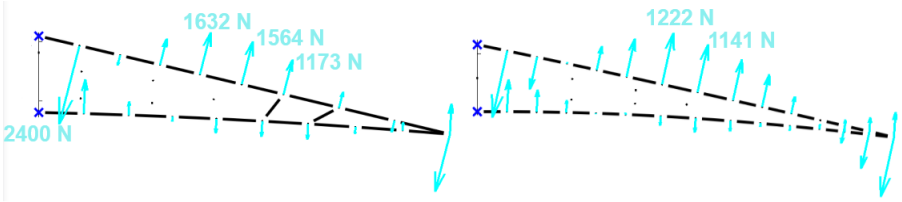

Figure 5.4: Aerodynamic load for inboard region reference section (left) and outboard region reference section (right).

In general terms, the outboard optimization is more critical due to the more reduced area between the lower and the upper skin and the fact that in this case, changes in the curvature between the original shape and the target shape occur near the tip end of the trailing edge, being the load paths unable to reach these points as it will be later on perceived. As a final remark before showing the results, it must be stated that in all cases a linear solver has been used, although in some cases a non-linear solver is

strongly recommended due to the high stress levels reached.

Finally, regarding the contour plots, only the stress distribution of the load paths has been represented. Since a beam model with an equivalent thickness is used to represent the rigidity of the skin, the stress distributions evaluated for it in the 2D model are not realistic.

5.2.1 Clamped trailing edge

The first trials have been done by considering the trailing edge to be clamped and both the skin and the load paths of the same material, in particular, aluminum alloy Al 7075-T6, with a Young modulus of 72 MPa and a Poisson's ratio of 0.33. Some results are shown in Figure 5.5, Figure 5.6, Figure 5.7 and Figure 5.8.

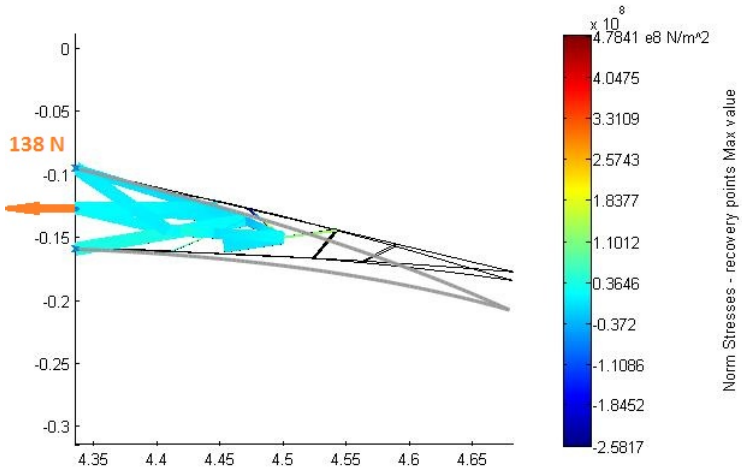

Figure 5.5: Pulling actuation solution for clamped trailing edge. Inboard region.

As it can be observed, these results are not convincing enough since. Due to the rigidity of the structure obtained only small deformations are allowed and consequently, shapes far from the target are achieved. In addition, some dints are observed, above all, in the lower skin when pushing actuation, probably due to the clamped boundary conditions as we can notice in Figure 5.9. To avoid these issues, flexible braces must be added at the tip end of the trailing edge, in such way that the shape is maintained in that area. As it will be later on observed, apart from the flexible braces, this problem can be solved as well by changing the boundary condition to a sliding

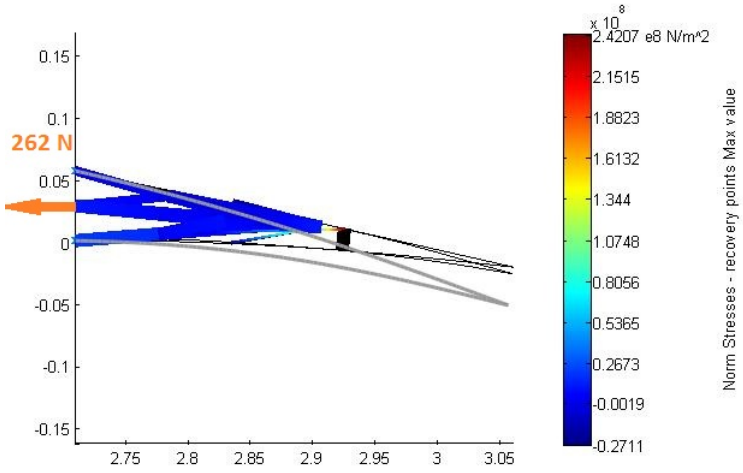

Figure 5.6: Pulling actuation solution for clamped trailing edge. Outboard region.

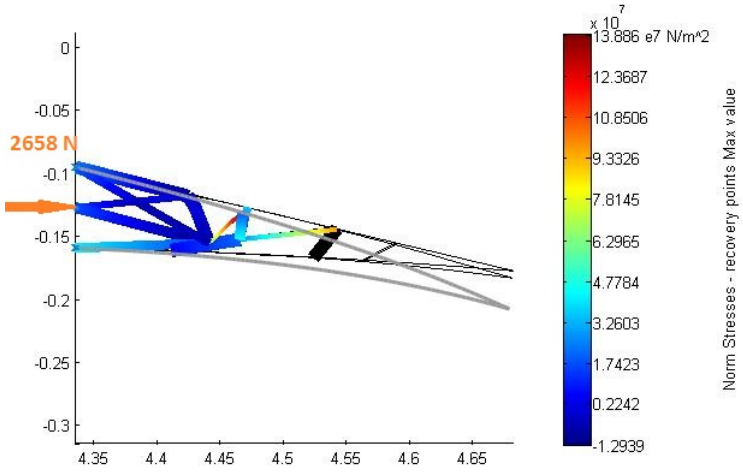

Figure 5.7: Pushing actuation solution for clamped trailing edge. Inboard region.

constraint in the lower skin. Also, heavier solutions with respect to the other ones afterwards presented are often found for this configuration. We can see in Figures 5.5, 5.6, 5.7 and 5.8 how many load paths are needed to deform the trailing edge downwards.

In spite of these undesiderable results, some useful studies were carried out during this part of the work concerning the qualitative behavior of the trailing edge. First

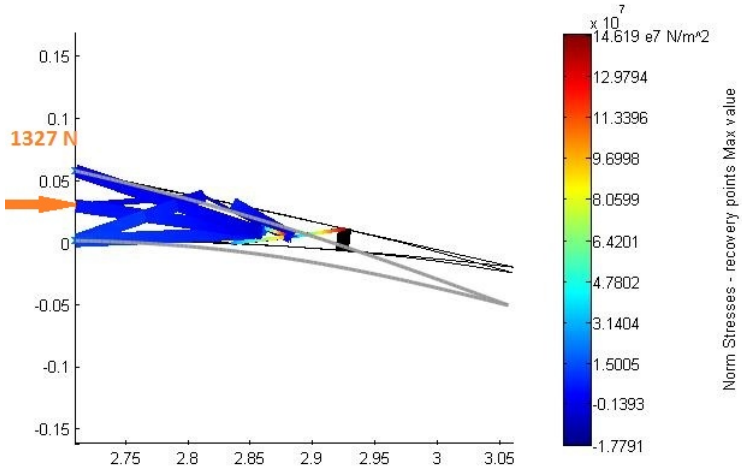

Figure 5.8: Pushing actuation solution for clamped trailing edge. Outboard region.

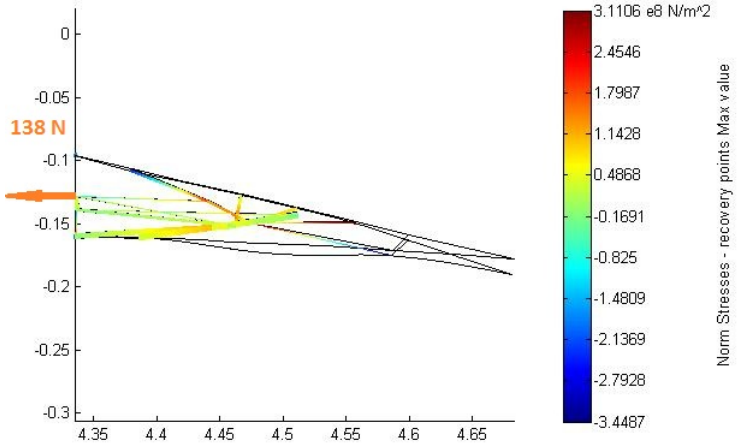

Figure 5.9: Inboard solution for single material clamped trailing edge. Dint in the lower skin.

of all, a sensitivity analysis on the position of the actuator was conducted. However, no remarkable differences were observed in the different solutions. Because of that, almost in all of the following studies we have considered a centered actuator.

Nevertheless, what it does have become very important in the subsequent studies, since it could be a driver for the final solution to be used in the real wing, is the behav-

ior of the trailing edge depending upon the performances of the actuator. As a matter of fact, in general it has been observed that as long as a clamped solution is considered a pulling actuation gives raise to a reduction of the actuation force (in some cases even of an order of magnitude), and the reduction in some manner of the shape irregularities already highlighted. This behavior could be driven by the fact that during pushing actuation the mechanism stiffens, or in some way gets stuck leading to less efficient actuation performance. As an example, it can be seen in Figure 5.7 how in case of the pushing actuation, we get a force that is more than ten times the force of the pulling actuation previously shown in Figure 5.5.

As it has already been stated the goodness of a solution is measured, in this work, in terms, not only of the shape achieved (LSE), but also in terms of actuation force requested and stress levels reached. In order to summarize the results obtained in these studies, in Table 5.1 they are shown the values of these magnitudes for the different configurations exploited in this section.

	LSE	Actuation force [N]	Maximum stress [Mpa]
Inboard (pulling actuation)	0.0098	138	478
Inboard (pushing actuation)	0.0094	2658	139
Outboard (pulling actuation)	0.0133	262	242
Outboard (pushing actuation)	0.0133	1327	146

Table 5.1: Summary results for clamped solution.

5.2.2 Double material

In order to make the structure more compliant without opening it in the lower skin the solution using different materials for the skin and the load paths have been investigated. In Figure 5.10 one can see a sensitivity study on the Young's modulus carried out in order to see better the qualitative behavior of the structure, although at the end, a material with a Young's modulus half the aluminum alloy's already used was chosen.

In light of the preliminary results coming from the sensitivity study; the solution adopted was as follows. For the tip end of the trailing edge the same behavior was observed and two flexible braces were added so as to better keep the shape in that area. For the first zone, instead, more points, apart from the ones given by the active

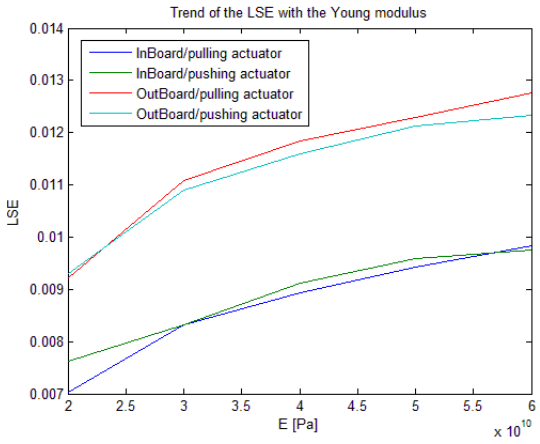

Figure 5.10: Behavior of the LSE with respect to the skin Young's modulus variation.

points optimization, were manually activated. In general, more active points along the skin permit a better control in the shape change. The results are shown in Figures 5.11, 5.12, 5.13 and 5.14.

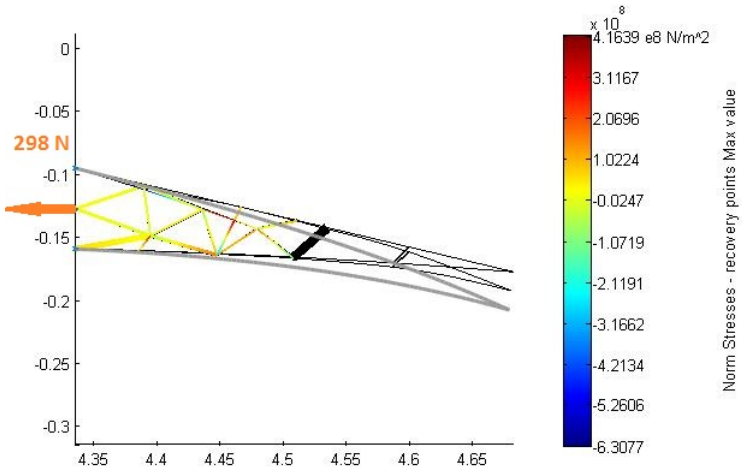

Figure 5.11: Pulling actuation solution for trailing edge with different materials for skin and load paths. Inboard region.

In this case we have a fully compliant structure, although deflection values yet far from the target curve can be achieved. In fact, it can be observed that only the tip end of the trailing edge is able to deflect downwards whereas the beginning of the

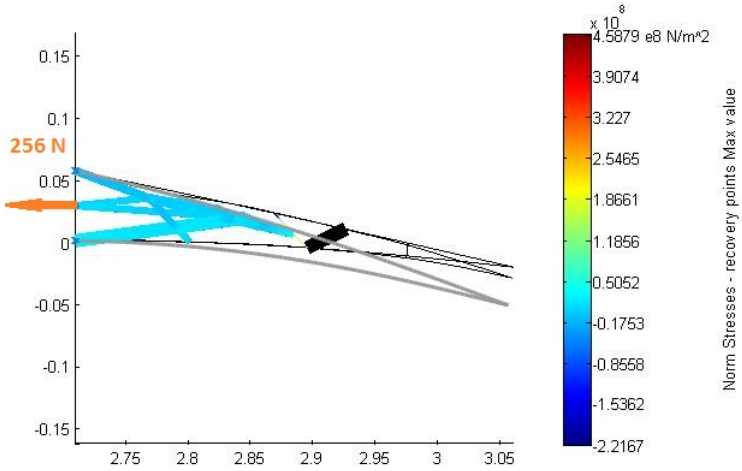

Figure 5.12: Pulling actuation solution for trailing edge with different materials for skin and load paths. Outboard region

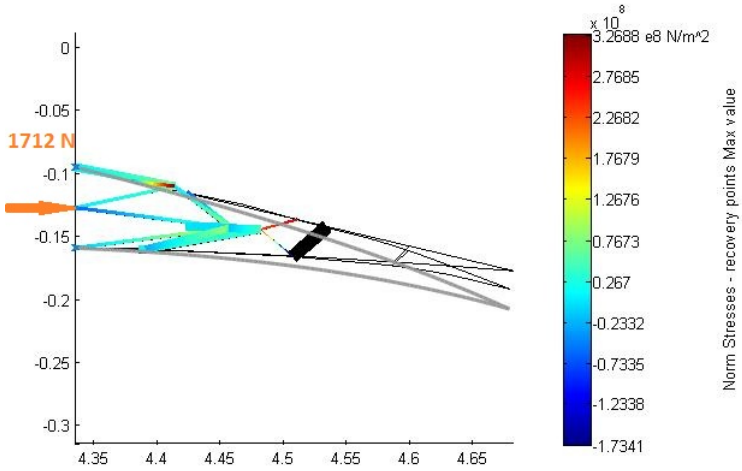

Figure 5.13: Pushing actuation solution for trailing edge with different materials for skin and load paths. Inboard region.

morphing region remains still. It is worth noting that as it happened in the single material clamped trailing edge whenever pulling actuation is considered lower input forces are needed to deflect the trailing edge downwards.

As it has been done in the previous case as well, in Table 5.2, the different values

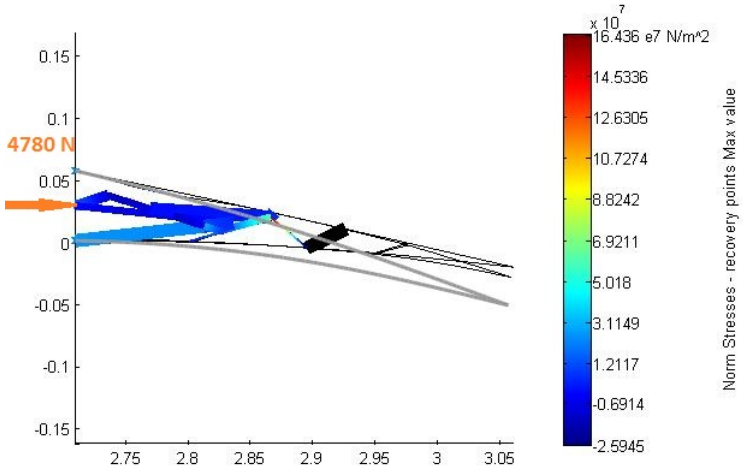

Figure 5.14: Pushing actuation solution for trailing edge with different materials for skin and load paths. Outboard region.

of LSE, actuation force and maximum stress reached, are shown so as to appreciate the different performances of the several configurations.

	LSE	Actuation force [N]	Maximum stress [Mpa]
Inboard (pulling actuation)	0.0080	298	416
Inboard (pushing actuation)	0.0083	1712	327
Outboard (pulling actuation)	0.0119	256	459
Outboard (pushing actuation)	0.0119	4780	164

Table 5.2: Summary results for double material solution.

5.2.3 Sliding constraint in the lower skin

In this case, the compliance of the structure comes from the alleviation of the constraint in the lower skin of the trailing edge where a slider has been placed. The results for both inboard and outboard regions are shown in Figures 5.15, 5.16, 5.17 and 5.18. Differently from what happens in the previous case, higher input forces are obtained for pulling actuation as it can be concluded from such Figures, although this difference is not as remarkable as in the clamped configuration.

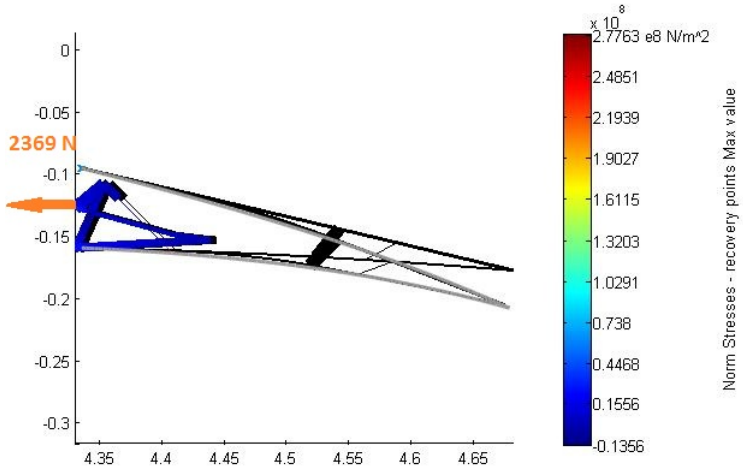

Figure 5.15: Pulling actuation solution for trailing edge with sliding constraint in the lower skin. Inboard region.

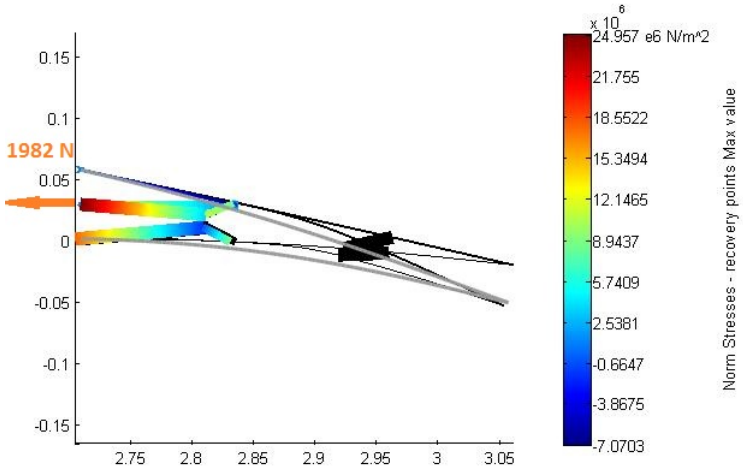

Figure 5.16: Pulling actuation solution for trailing edge with sliding constraint in the lower skin. Outboard region.

In this case, especially for inboard region, deformations very close to the target curve are obtained, being the outboard region design always more critical. Another issue that has been observed is the fact that a stiffer behavior is obtained as long as pushing actuation is considered. It can be checked by evaluating the displacement of

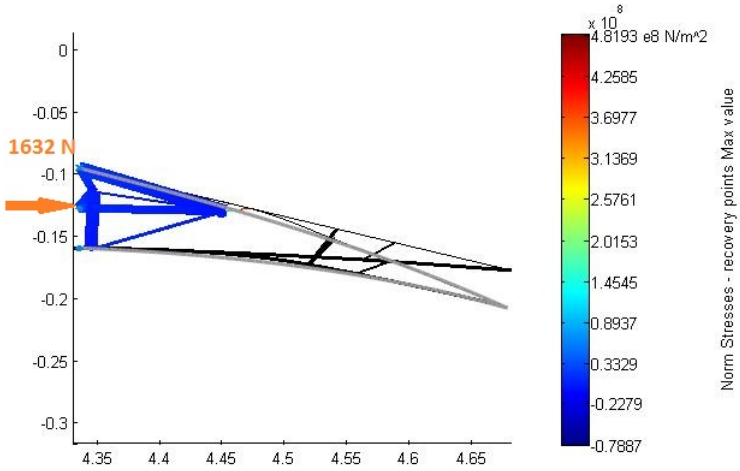

Figure 5.17: Pushing actuation solution for trailing edge with sliding constraint in the lower skin. Inboard region.

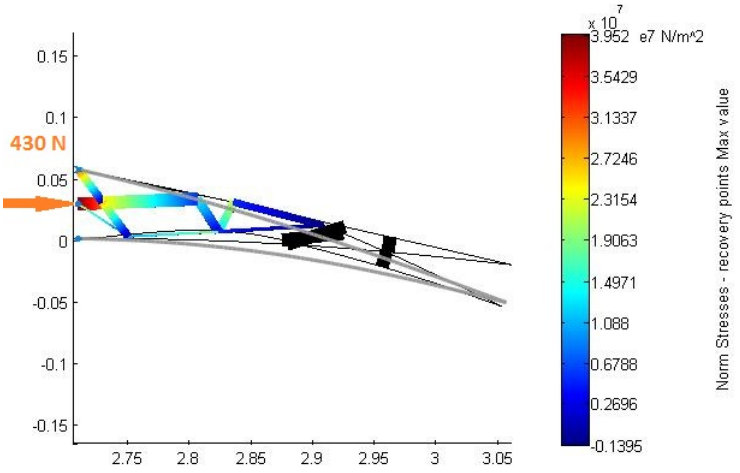

Figure 5.18: Pushing actuation solution for trailing edge with sliding constraint in the lower skin. Inboard region.

the actuation point for each case (Table 5.3).

Finally, more compliant solutions can be observed since variations in the normal stress of some order of magnitude occur in some cases, although not a fully compliant

	Pushing actuation	Pulling actuation
Inboard	$1.147e-5m$	$-0.0047m$
Outboard	$2.034e-6m$	$-0.0043m$

Table 5.3: Comparison of input point displacement depending upon the performance of the actuation.

structure can be obtained since it has to be opened in order to avoid either high stress levels or irregularities in the skin deformation.

To sum up, the values of LSE, actuation force, and maximum stress obtained in this case are reported in Table 5.4.

	LSE	Actuation force [N]	Maximum stress [Mpa]
Inboard (pulling actuation)	0.0049	2369	278
Inboard (pushing actuation)	0.0050	1632	482
Outboard (pulling actuation)	0.0055	1982	25
Outboard (pushing actuation)	0.0068	430	39

Table 5.4: Summary results for sliding constraint solution.

5.2.4 Actuation in the lower skin sliding constraint

The last solution that has been investigated is putting the actuation force directly in the sliding constraint of the lower skin. Such solution seemed to be very promising "a priorit't', and as a matter of fact the deformations reached in this case were the best that far achieved with respect to the target curve. In Figure 5.19 and Figure 5.20 it can be perceived how in terms of deformations this solutions are optimal even for outboard region.

Nevertheless, the weakest point of this solution is the actuation force. We can see that the fact that the input point is directly attached to the lower skin hinders the creation of a mechanism complex enough to diminish the force. However, this has helped us in realizing how efficient a potential compliant mechanism for a real trailing edge could be in reducing the actuation, for, as already seen very low input forces can be achieved in some cases. Besides, higher stress levels are reached in this case with respect to the former ones, especially in the inboard region even exceeding the aluminum tensile yield strength.

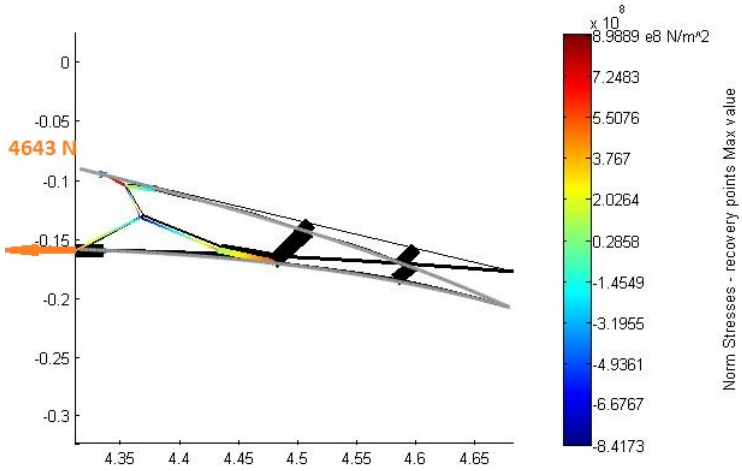

Figure 5.19: Solution for the case of input force actuating in the sliding constraint. Inboard region.

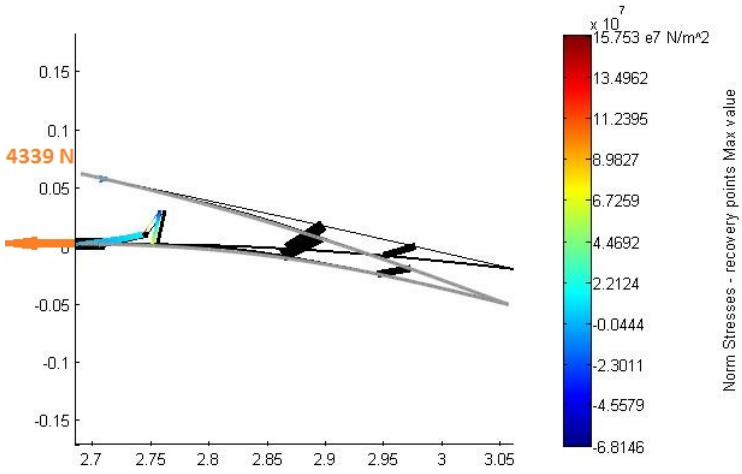

Figure 5.20: Solution for the case of input force actuating in the sliding constraint. Outboard region.

As well as it has been done in the former cases, also in this one, it may be observed in Table 5.5, the values obtained of the magnitudes of interest.

	LSE	Actuation force [N]	Maximum stress [Mpa]
Inboard	0.0037	4643	899
Outboard	0.0034	4339	157

Table 5.5: Summary results for actuation in sliding constraint solution.

5.2.5 Conclusions

The conclusions coming from these preliminary studies are summarized in what follows:

- The outboard region design is more critical due to the fact that the reduced space and the fact that active points are close to its tip end makes it difficult for the load paths to reach them.
- As long as a single material is considered with clamped constraint poor deformation levels can be achieved and heavy and no compliant solutions are obtained.
- In the case of clamped trailing edge, lower actuation forces are needed when pulling actuation is considered together with more regular shapes of the deformed trailing edge.
- In the case of the sliding constraint, deformations closed to the target shapes are obtained.
- The behavior of the actuation performance reverses in the sliding constraint case.
- At least one flexible brace is necessary in order to keep the shape at the tip end of the trailing edge.
- Active points must be carefully activated so as to keep a good control in the shape change. The solution is highly dependent on this issue.

5.3 Multiobjective studies

As already explained, the synthesis of compliant mechanisms is defined as the design of a structure able to convert a displacement or a force in order to efficiently transfer the deformation work from an input point (actuator) to one or more output points with different directions. Since this is only a kinematic requirement, additional structural

requirements must be added because by definition, compliant mechanisms work in the elastic domain. In order to design a compliant mechanism able to meet both kinematic (motion) and structural (load-carrying) requirements, the design is decomposed into several parts considering the mechanism design and the structure design, respectively, for a corresponding number of load conditions. These design problems are combined by incorporating a multiobjective optimization, based on the concept of Pareto domination, in the genetic optimizer. The Pareto-optimal set of resultant fitnesses is a set of solutions such that it is not possible to improve any objective without, at the same time, worsening another. In such case all the other solutions are dominated by these better ones and they can be discarded. In this way, to design compliant mechanisms tries to combine the need for flexibility as well as structural stiffness.

In the SIMO problems, the objective function to be minimized is the Least Square Error (LSE) between the deformed curve and a target curve, as described in the Equation 5.1. In general, more than one load conditions for the target curve corresponding to the undeformed airfoil and more than one morphing target curves with corresponding external loads can be taken into account. In this case the same set of loads but different set of boundary conditions is considered. The idea is to keep the undeformed shape when no load is applied, so the problem can be set up as follows:

1. Kinematic requirement: the Least Square Error is minimized in order to match the deformation with the target curve under the loads given by the flight condition so far considered (cruise condition) with the following constraints: clamped upper skin and slider in the actuation point. For the lower skin, depending on the case, we will consider it to be either clamped or with a slider.

2. Structural requirement: in this case the Strain Energy is minimized under cruise flight condition loads with constraints as follows: clamped upper skin, actuation point, and lower skin.

The structural topology which minimizes the LSE is one that maximizes the potential energy [21] equal to the virtual work needed because the direction and orientation of the output points allow to match the displacements required by the desired morphing shape, under the input actuation load and the external aerodynamic loads corresponding to a given flight condition.

The second part of the two-part problem is the structure design which in the SISO problem employs the simplest type of design problem formulation in the topology op-

timization field, namely minimum compliance design (maximum global stiffness) [23]. Minimizing the LSE between the deformed curve and the target curve corresponding to the undeformed airfoil allows accounting for the resistance of the work piece.

In this case, based on the results obtained in the previous studies we have focused on the the solutions of the sliding constraint, the two materials, and a combined solution of the other two. Another consideration that has been made during this study is that, once we have realized how low the actuation force that can be obtained in some cases is, the boundaries in which the actuation force can vary during the optimization procedure have been diminished. Also, the boundaries of the thickness of the skin and the load paths have been lowered so as to get lighter solutions, and thus more compliant.

5.3.1 Double material

In this solution, as already explained in the single objective studies, a material with a Young's modulus equal half that of aluminum and clamped on lower and upper skin is considered. In Figures 5.21 and 5.22 we can see the results for both inboard and outboard cases. It is worth noting the low input forces needed to deform the structure together with the high values of stress level reached in some load paths. In addition, the deflection values achieved in this case are still far from the desired one. These facts evidence that the clamped boundary condition is not an optimal solution for this trailing edge not only in terms of LSE, but also because of the higher stresses reached with respect to the other cases.

As far as the deflection behavior is concerned, we can see in Figure 5.23 that this is linearly decreasing , although only low values can be reached. In fact it can be noticed that very small variations of the equivalent deflection angle can be obtained when varying the input force. This gives us an idea of the rigidity of the structure even considering a more flexible material for the skin. This rigidity of the structure can be observed as well in the fact that remarkable deformations are only reached in the tip end, and the initial part of the structure being almost still.

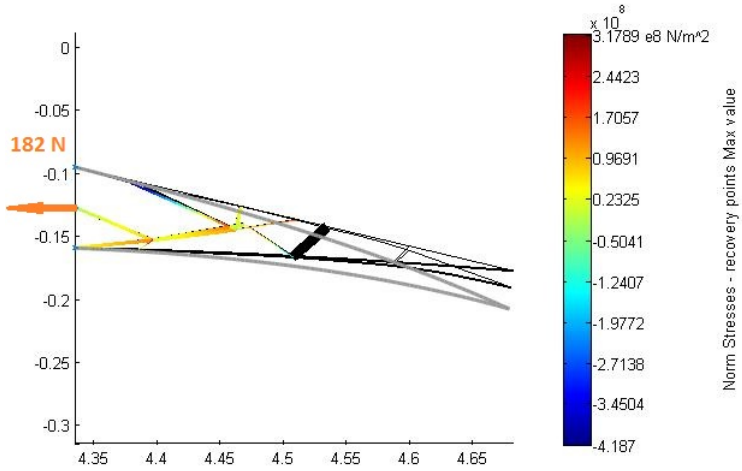

Figure 5.21: Double material solution for the case of double material configuration. Inboard region.

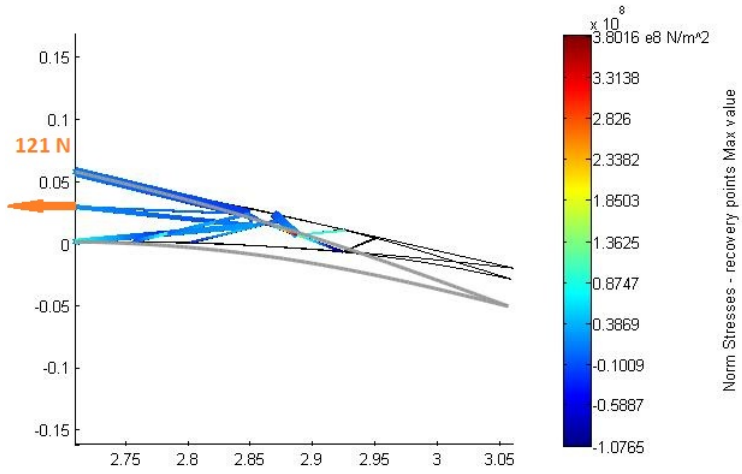

Figure 5.22: Double material solution for the case of double material configuration. Outboard region.

5.3.2 Sliding constraint in the lower skin

In this case aluminum alloy has been considered for both load paths and skin. As we can see in Figure 5.24 and Figure 5.25 good deformations levels close to the target shapes are obtained. Nevertheless, it can be observed that in some cases the higher

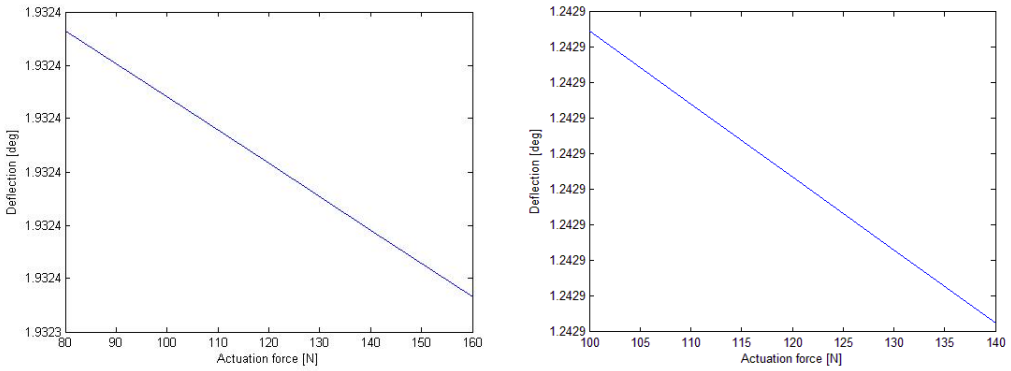

Figure 5.23: Equivalent deflection behavior for double material configuration. Inboard (left) and outboard (right).

stress levels overcome the yield strength of Al (503 MPa). Thus, in this case a non-linear solver is strongly needed in order to get realistic results. It has been observed that the lower the input force is the higher are the stress levels in the load paths and thus the more the compliant mechanism must work in order to get desirable deformations.

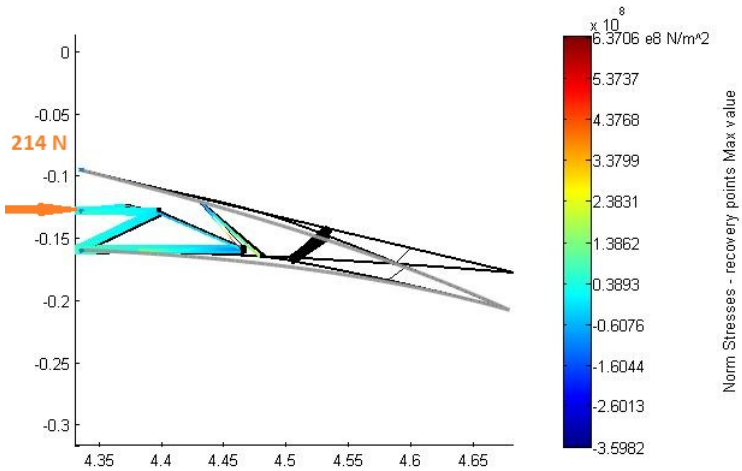

Figure 5.24: Inboard solution for sliding constraint configuration. Pushing actuation.

In this case also some studies on the deflection behavior have been carried out. For the sliding constraint configuration although the behavior being also linear the trend

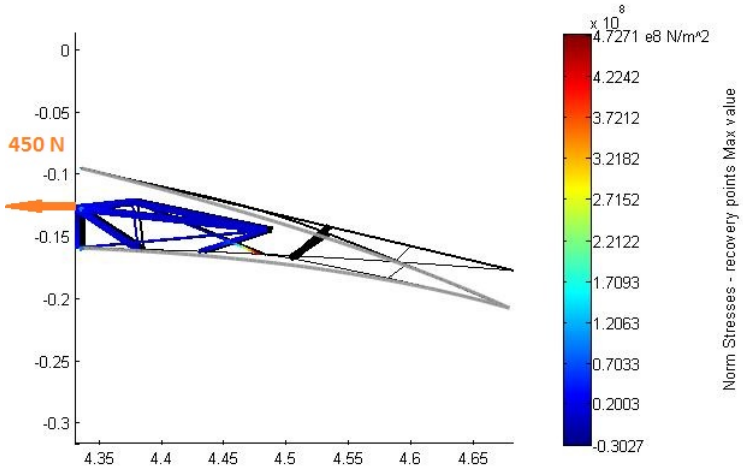

Figure 5.25: Inboard solution for sliding constraint configuration. Pulling actuation.

changes with respect to the clamped configuration case. In addition a more compliant behavior is observed since higher deflection changes are obtained when varying the input force.

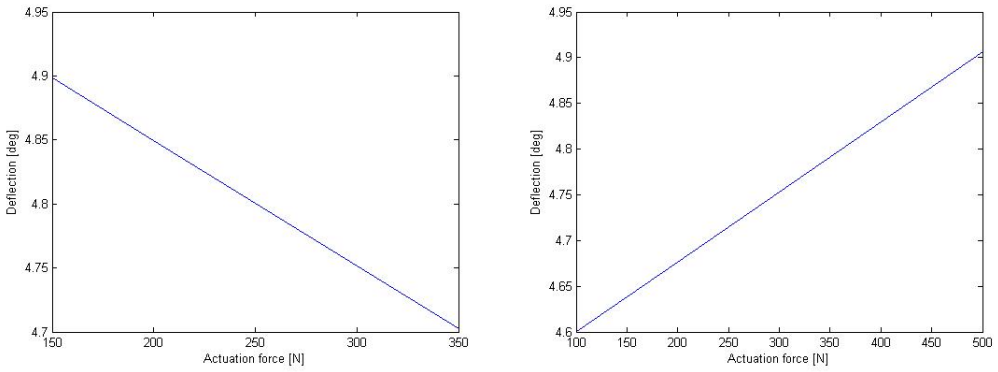

Figure 5.26: Equivalent deflection behavior for slider and single material configuration. Pushing actuation (left) and pulling actuation (right).

5.3.3 Double material with sliding constraint in the lower skin

Finally the same studies already presented for a combined solution between the other two have been carried out. Let us first consider the inboard region. As it can be seen

from Figures 5.27 and 5.28 good deformations have been obtained in this case together with acceptable stress values. Regarding the deflection behavior it has been observed the same as the previous case and a major flexibility when pulling actuation is considered together with a closer approach to the desired value (5º). Nevertheless, in this case higher input forces are required.

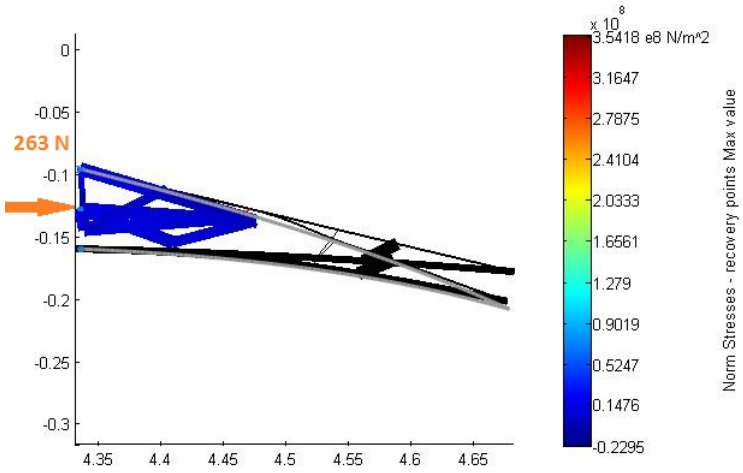

Figure 5.27: Inboard solution for sliding constraint with different materials for skin and load paths. Pushing actuation.

It is worth noting that the same behavior regarding the stress level reached is observed depending on the actuator performance. The lower the actuation force is the more the compliant mechanism must work and thus higher stress levels are reached.

For the outboard region the same studies have been carried out with similar conclusions as to the inboard solutions. As usual in this case the design is more critical, being unable to reach LSE's comparable to the ones of inboard region, although lower than in other cases. However, high deflection values, close to the target ones can be reached. As far as the stress levels are concerned, these are quite acceptable and uniform distributions are obtained.

Due to its good compromise in terms of LSE, actuation force requested and maximum stress reached in the future 3D validation studies, a solution based on this configuration have been adopted.

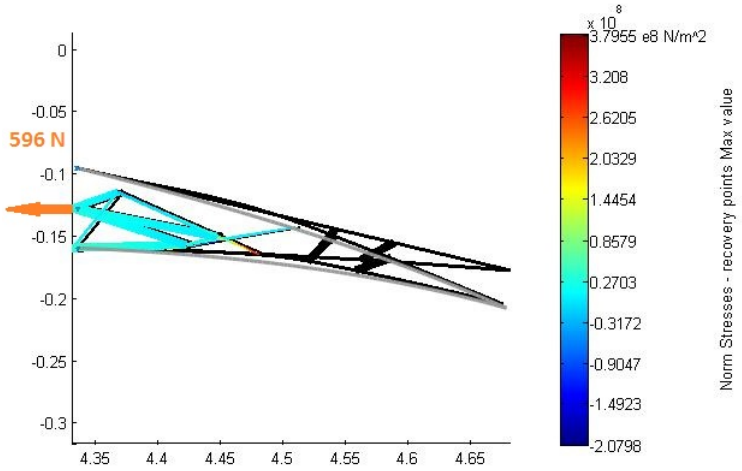

Figure 5.28: Inboard solution for sliding constraint with different materials for skin and load paths. Pulling actuation.

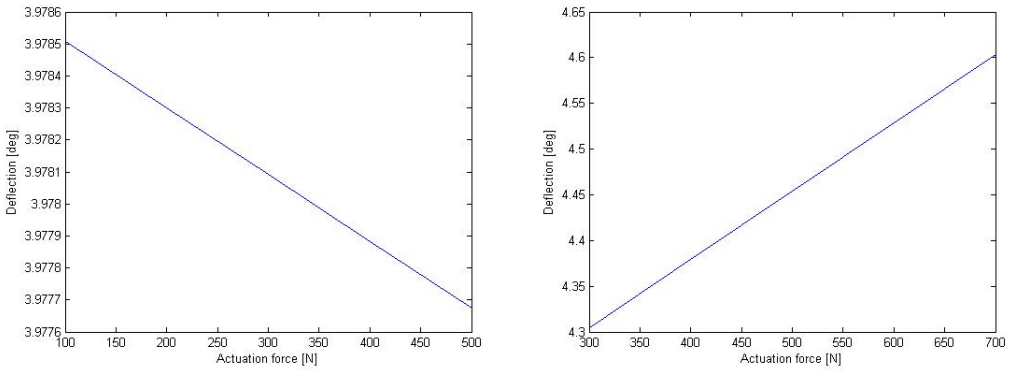

Figure 5.29: Equivalent deflection behavior for slider and double material configuration. Pushing actuation (left) and pulling actuation (right).

5.3.4 Conclusions

From these multiobjective studies it can be concluded that:

- As long as clamped trailing edge is considered, low deflection values can be reached even considering a more flexible material for the skin.
- The behavior of the deflection highly depends on the configuration. Indeed, opposite behavior is observed for clamped and sliding constraint solutions.

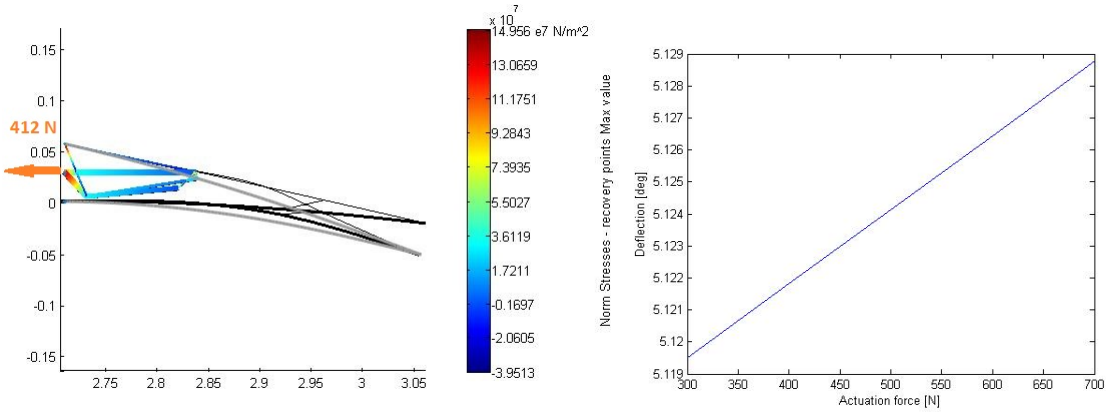

Figure 5.30: Outboard solution for sliding constraint with different materials for skin and load paths and deflection behavior.

- Good solutions in terms of deformations can be achieved as long as sliding constraint is considered, for both single and double material configurations.
- Acceptable stress levels are reached in all cases.
- The lower the actuation force is the more the compliant mechanism must work and thus higher stress levels are reached.

In order to summarized the results obtained in these studies, and for the sake of clarity, in Figure 5.31 it is shown a superposition of the Pareto front corresponding to the different solutions above explained. The first thing that is worth saying is the improvement of both objectives as long as a slider is placed in the lower skin. Regarding the slider solutions, in spite of the smaller differences, it may be observed an improvement, in particular of the LSE, whenever the different materials are considered, reaching values of almost $4 \cdot 10^{-3}$ for pulling actuation.

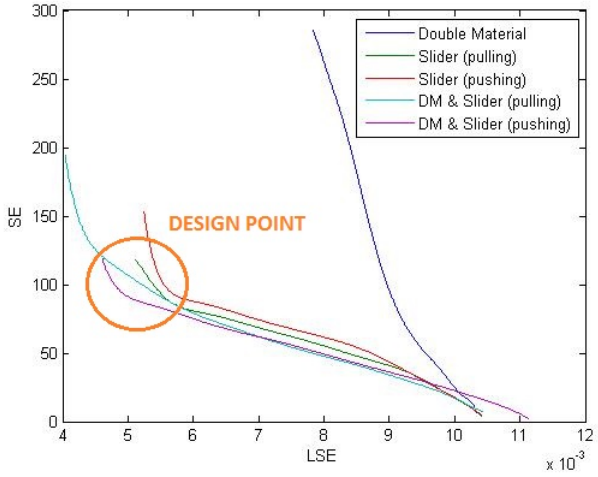

Figure 5.31: Pareto front plot for the different solutions.

Chapter 6

3D morphing wing validation studies

Once each region of the reference wing has been optimized in this chapter, two validation tests of the solutions previously found have been performed. To do so, after identifying the position of the adaptive ribs, it has been carried out an extension of the solution found for each region maintaining the same configuration.

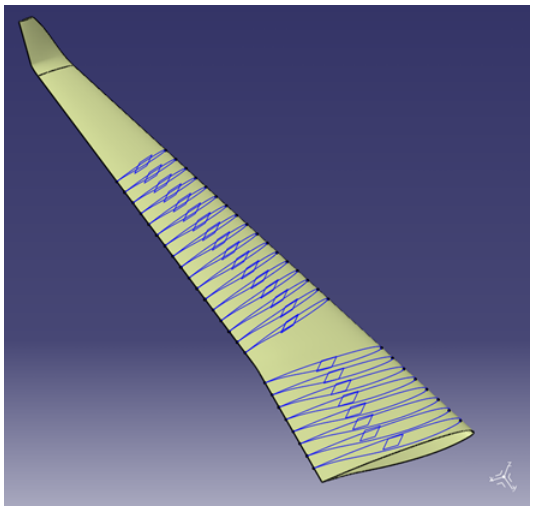

Figure 6.1: Position of the adaptive ribs in the 3D wing.

6.1 Extension of the optimized solutions

The first step in the extension of the solution has been identifying the adaptive ribs. A set of eight adaptive sections for inboard and seventeen for outboard region were extracted from the CAD of SARISTU reference wing each one spaced $440mm$ in span-wise direction. In Figure 6.1 we can see the position of the compliant ribs.

By using the already explained PHORMA tool for airfoil representation, the shapes of the sections have been represented as CST objects so that they could be handled by the code.

As far as the extension of the proper solution is concerned, the curvilinear coordinate of the points along the skin has been preserved as well as the proportional distance between the internal points and the upper and lower skins. As already mentioned in section 2.1.4, the stiffness of the skin is represented by beam elements with an equivalent thickness during the 2D optimization process. However, in order to obtain the real thickness of the airfoil skin a model based on the calculation of its bending stiffness considered as a plate has been used[2]:

$$t_{skin} = \sqrt[3]{\frac{w_{rib}}{p_{rib}}} t_{beam}$$

where t_{skin} and t_{beam} are the thickness of the 3D wing skin and the thickness of the equivalent beams representing the skins in the 2D beam model used during the genetic optimization, respectively, w_{rib} is the rib thickness, in the span-wise direction. that in our case is $0.012m$ and p_{rib} is the rib pitch, $0.44m$ in this case.

In order to model the hinge corresponding to the attachment of the wing box to the fuselage two nodes where created connected by rigid elements RBE2 to the front and rear spars as we can be see in Figure 6.2.

In this trailing edge morphing configuration it happens that the beginning of the morphing region does not coincide with the position of the rear spar, thus after collocating the adaptive ribs in their correspondent place, perpendicular to it, it was decided to attach the upper skin to the wing box by means of rigid elements RBE2 and the same for the lower skin but allowing the displacements in the horizontal plane. The result can be seen in Figure 6.3.

Besides, four omega-section stringers were added in the upper skin where the load paths reach the skin. From a constructive standpoint, the stringers are used to give support in the attachment points of the load paths and the skin. In addition, they help

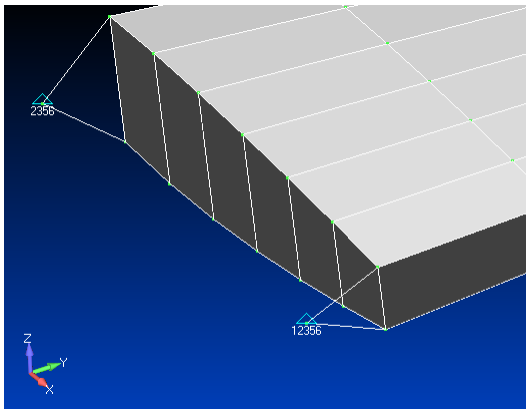

Figure 6.2: Constraints application.

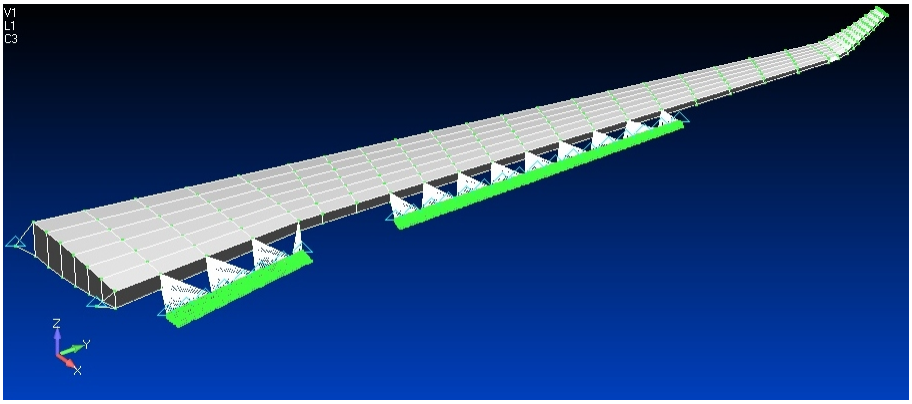

Figure 6.3: Attachment of the morphing trailing edge to the wing box by means of rigid elements RBE2.

in distributing the deformation in a uniform way along the span-wise direction.

As far as the aerodynamic loads application is concerned, a chord-wise varying pressure has been applied following the same distribution law of the 2D models as it can be see in Figure 6.5. However, for the wing box a different approach has been adopted. The internal forces have been applied in the ribs of the wing box with the help of RBE3 elements as it is shown in the right image of Figure 6.5. In Figure 6.6 it is reported the internal forces distribution along the span-wise direction for the load case here considered.

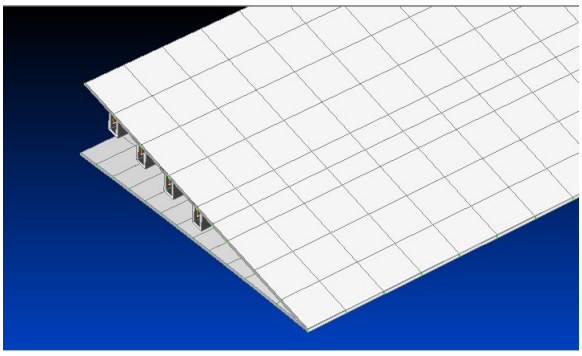

Figure 6.4: Stringers in load paths connections with the upper skin.

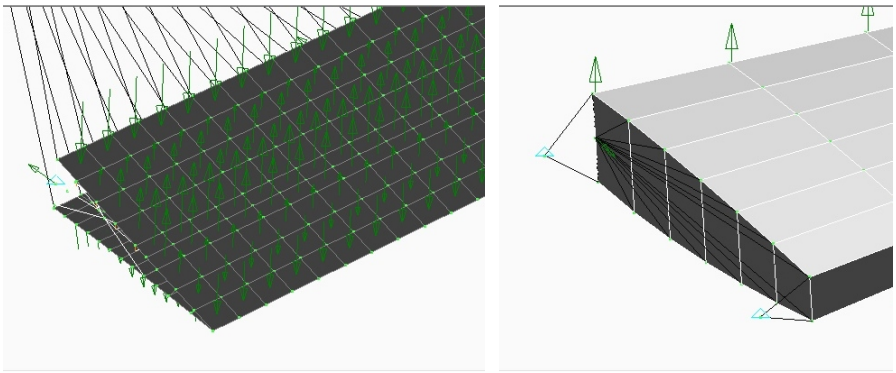

Figure 6.5: Aerodynamic loads application.

6.2 First validation test

For this first validation test the solutions that are shown in Figures 6.7 and 6.8 were chosen for inboard and outboard region respectively. The three main drivers to prune the different solutions were the deformation obtained measured as Least Square Error with respect to the target curve, maximum stress levels reached and actuation force.

As it has been already explained there is not a solution that is optimal for all the three criteria since for instance very low input forces may give raise to very stressed compliant structures but good deformation behavior or solutions that are good in terms of LSE and stress levels, require an extremely high actuation performance. The solutions here exploited must be seen as a trade-off between the former drivers. The maximum stress levels reached in them are far below the yield tensile strength of the aluminum alloy used for the characterization of the load paths. In addition, good de-

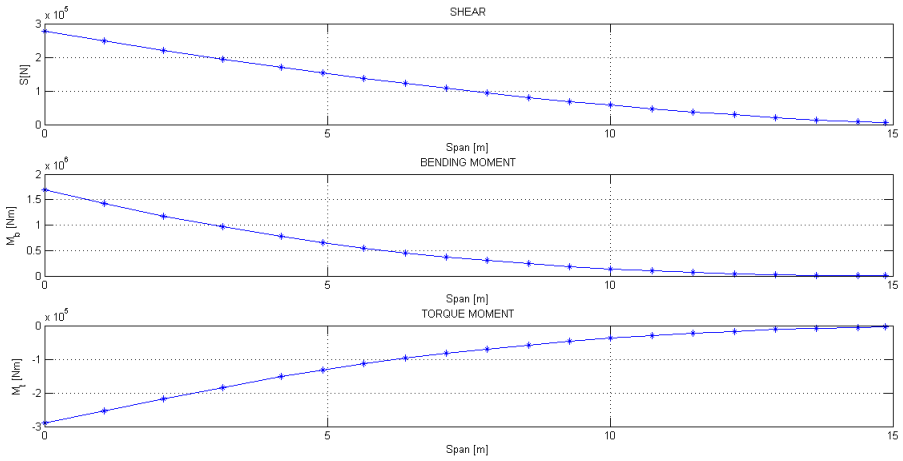

Figure 6.6: Internal forces distribution in span-wise direction for Load Case 1.

formation behavior is achieved, although it always worsens in outboard region due to its intrinsic peculiarities, and acceptable actuation forces are requested.

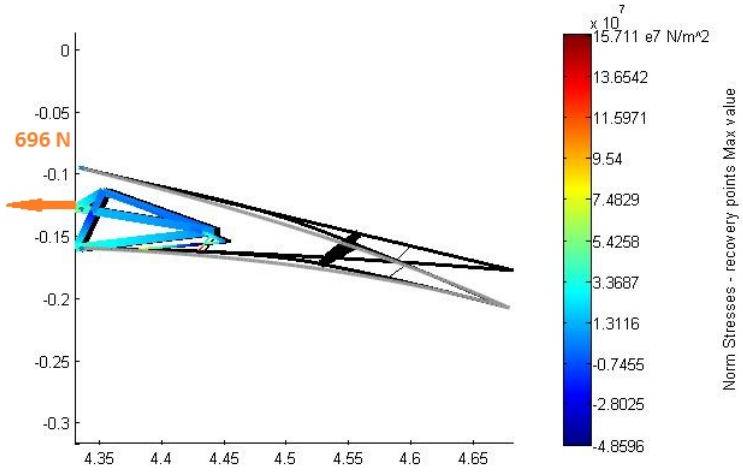

Figure 6.7: 2D inboard solution for the first validation test.

The 3D model has been built with an upper and lower skin of 1.6mm and 3.6mm in outboard region and 4mm for both of them in inboard region. The linear static analysis

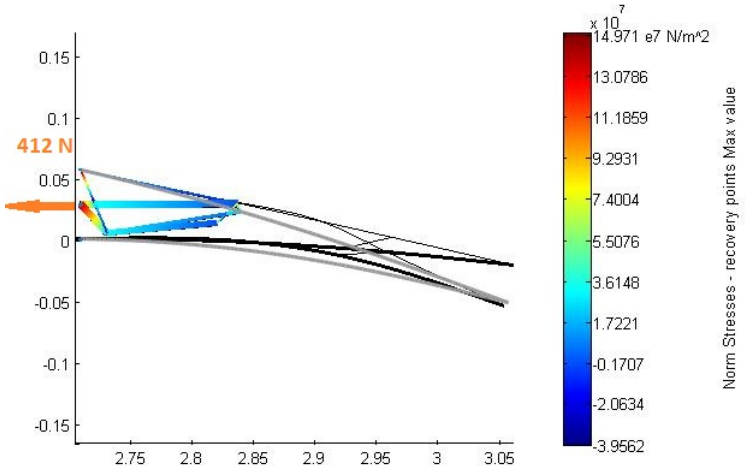

Figure 6.8: 2D outboard solution for the first validation test.

have been performed using MSC/NASTRAN Software with the same actuation force coming from the 2D optimized models.

In which follows, the results of the analysis considering a chord-wise pressure applied in the skin are shown. In Figure 6.9, it can be perceived a contour plot of the VonMisses stress distribution in the skin. Thanks to the stringers a uniform distribution of the stress can be obtained in span wise direction, although in outboard region the results worsens. Some stress concentration zones can be perceived probably due to the rigid attachment of the morphing trailing edge to the wing box by means of the rigid elements. As far as the deformation is concerned, good behavior in chord-wise direction is obtained, in particular in inboard region. However, in outboard region, some irregularities can be observed in correspondence with the adaptive ribs position. This issue could be observed as well in the 2D model, thus, it is probably due to the solution chosen for the extension. Finally, a comparison between the rib placed in station four for different models is reported. As it can be noticed, the use of the stringers does not affect the deformation in chord-wise direction, although they are mandatory in order to improve the deformations in span-wise direction. It is worth mentioning the stiffer behavior of the 3D model. As a final remark, it must be said that a reduction of the stress reached has been observed compared to the 2D models both in the skin and the load paths.

Since the 2D solution used in this validation test comes from a multiobjective study

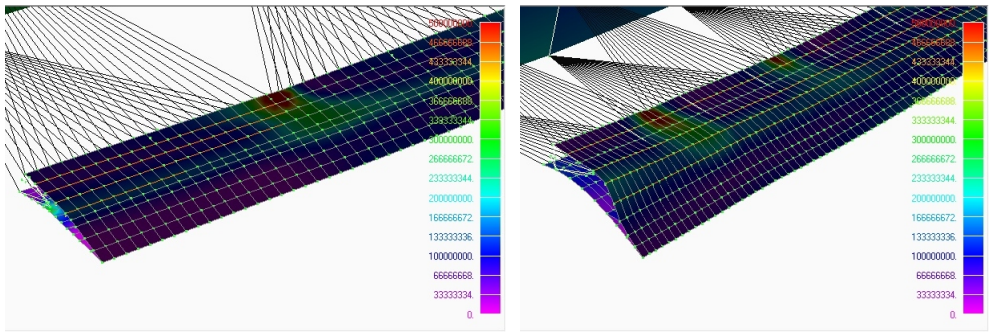

Figure 6.9: VonMisses stress $\left[\frac{N}{m^2}\right]$ contour plot for downwards deflection in the first validation. Inboard region (left) and outboard region (right).

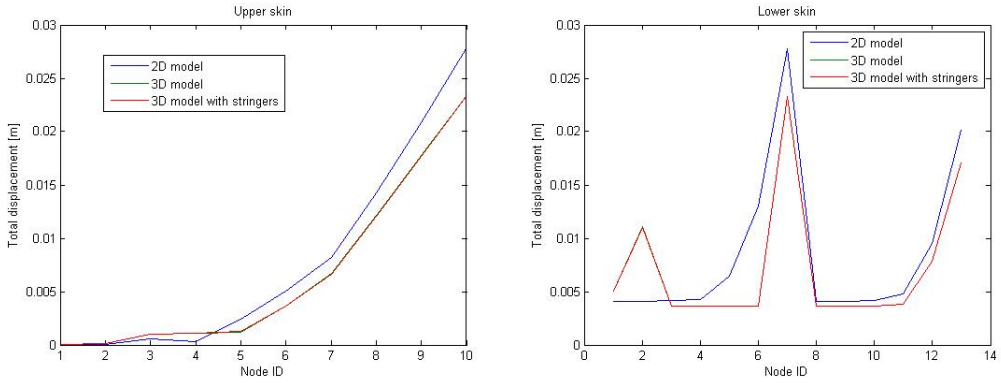

Figure 6.10: Comparison of the displacements for the adaptive rib in station 4 according to different models of the first validation test.

in which the second objective represents a structural requirement, it also has been carried out an analysis in which both the lower skin and the actuation point are blocked. The contour plot of Figure 6.11 show the results of this analysis. The structural requirement is mostly fulfilled in inboard region, although some irregularities are again observed in outboard region, again probably due to the solution chosen. In this case, higher stress levels are reached with respect to the former analysis.

In addition to the later considerations, in general terms, an order of magnitude higher constraint forces, as compared to the actuation forces requested for downwards deflection, are required for the fulfillment of the structural requirement as it is eminent from Figure 6.12. This is probably due to the priority given to the first objective (LSE), in the selection of the point in the Pareto front, meaning that the mechanism is more

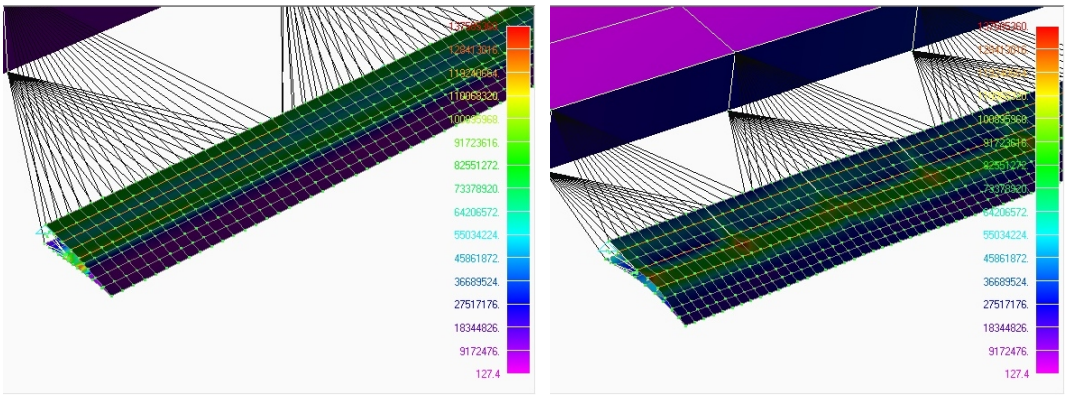

Figure 6.11: VonMisses stress $\left[\frac{N}{m^2}\right]$ contour plot for structural requirement check in the first validation test. Inboard region (left) and outboard region (right).

efficient when deflecting the trailing edge than when blocking it. In addition to this, in incoming project phases it will be needed to add a blocking system so that the actuation do not work when it is necessary to keep the trailing edge's shape.

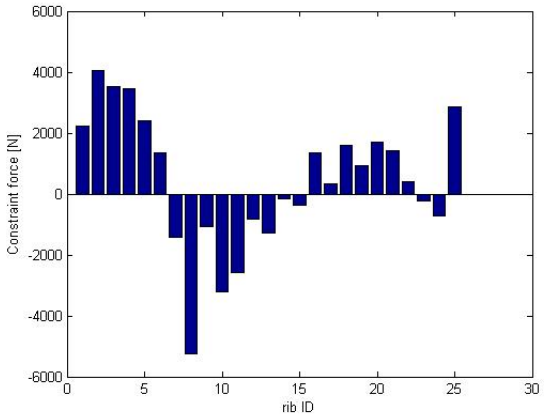

Figure 6.12: Constraint force for mechanism locking in the first validation test.

6.3 Second validation test

In order to improve the results obtained in the previous solution, another validation test has been performed, this time with the same configuration for both regions but with a better solution in terms of deformation (LSE) and connectivity. It is shown in

Figure 6.13 and it can be seen load paths attached to four points in the upper skin and one in the lower skin whereas they reached only two points in the lower skin in the previous section's solution. The actuation force is even lower in this case, but the maximum stress value reached exceeds the Al-7075 tensile yield strength. Nevertheless, it was observed in the previous studies that the stress values in the 3D model decreased of about a 30% with respect to those in the 2D models.

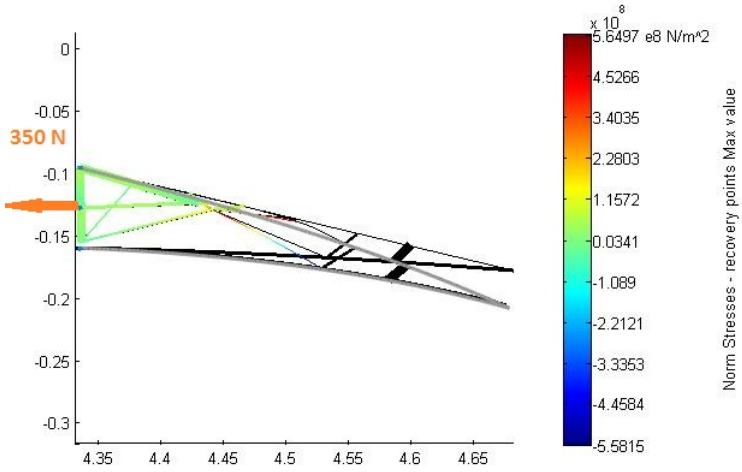

Figure 6.13: 2D solution for the second validation test

As done in the former section, a validation static linear analysis was performed with the same actuation forces of the 2D model. In this case, the thickness of the 3D model skin is 1.5mm for the upper skin and 3.6mm for the lower skin.

The first analysis regards, as done in the previous case, the case in which chordwise varying pressure is applied on the skins. Figure 6.14 shows the results for this first analysis. In inboard region, it can be observed a quite uniform stress distribution and good deformation behavior, although, in Figure 6.15, one can see that, in this case, a lower deflection value is achieved. Because of this, a higher input force is required in order to obtain the desired deflection. As far as outboard region is concerned, it can be observed that a more connective solution make the irregularities of the previous validation test disappear. However, since the solution used in this one has not been optimized for this region, deflection values far from the target are achieved.

As it also has been done in the first case, it is reported here a comparison of the nodal displacements of the rib placed in station four of the different models. In this

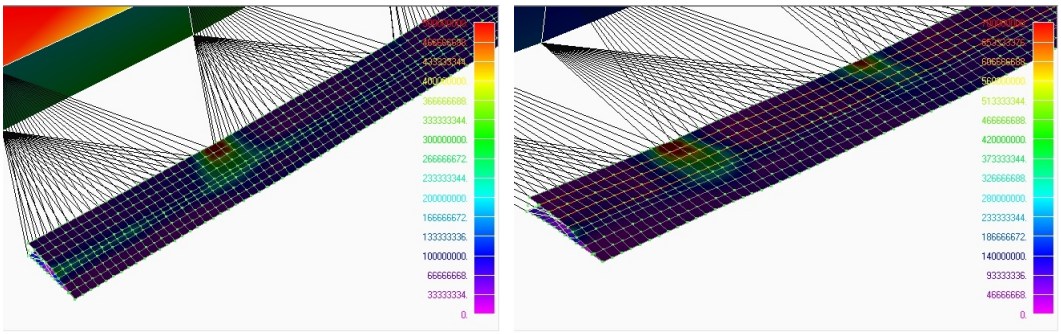

Figure 6.14: VonMisses stress $\left[\frac{N}{m^2}\right]$ contour plot for downwards deflection in the second validation test. Inboard region (left) and outboard region (right).

model it has been observed an improvement also in chord-wise direction thanks to the stringers, although an even stiffer behavior of the 3D model is obtained as compared to the model of the previous validation study.

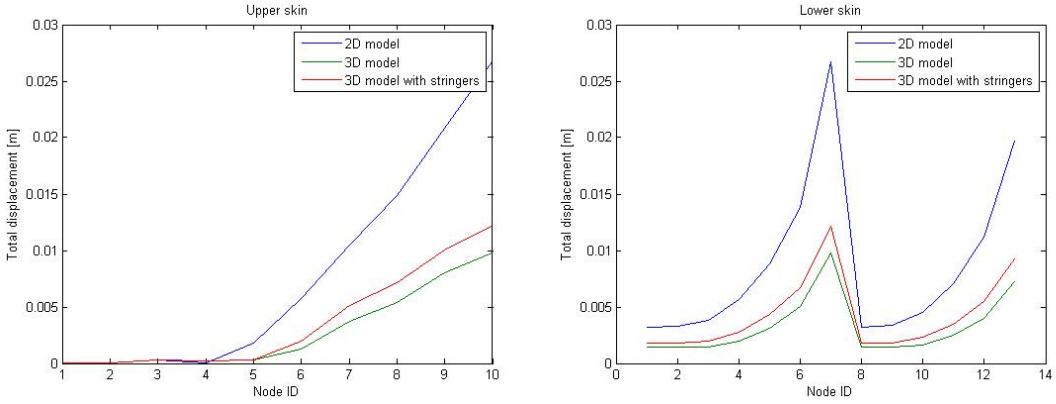

Figure 6.15: Comparison of the displacements for the adaptive rib in station 4 according to different models of the second validation test.

With this solution, thanks to its better connectivity, the structural requirement is fulfilled both in inboard and outboard regions as it can be noticed in Figure 6.16. The more connective solution makes the strain energy be distributed in a more efficient way within the compliant mechanism. However, the constraint forces requested in this case are again, for some ribs, an order of magnitude higher than the ones required to deflect the trailing edge downwards as one can observe in Figure 6.17, again probably because of the priority given to the LSE.

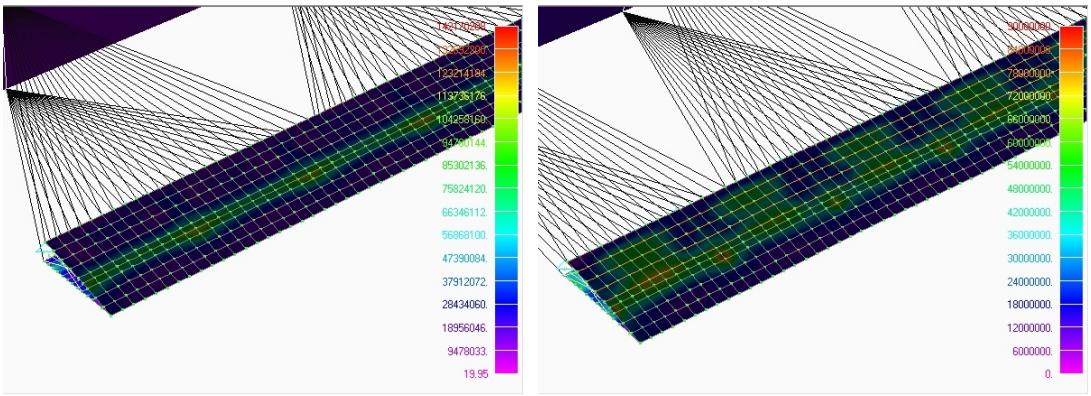

Figure 6.16: VonMisses stress $\left[\frac{N}{m^2}\right]$ contour plot for structural requirement check in the second validation test. Inboard region (left) and outboard region (right).

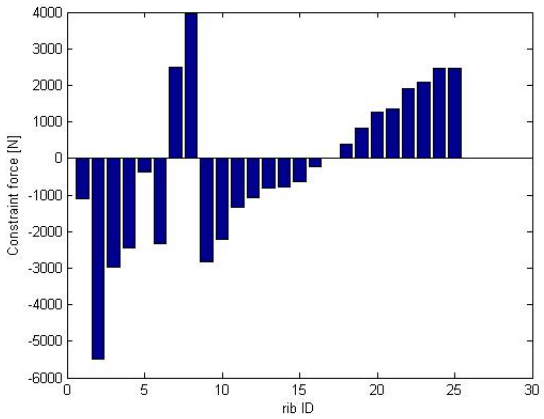

Figure 6.17: Constraint force for mechanism locking in the second validation test.

6.4 Conclusions

As a general conclusion it can be said that in the validation studies it has been found both good deformation behavior and acceptable stress levels. In addition, it has been proved the capacity of this kind of structure to give support aerodynamic loads, maintaining the airfoil undeformed shape.

One of the most important issues to be taken into account in the design of compliant mechanisms is the connectivity of the solution. More load paths attached both to the upper and lower skin permit a better control and a complete fulfillment of the

structural requirement, since the strain energy is more efficiently spread within the compliant structure. Finally, as already said, it future phases of the project, a blocking system to maintain the shape of the trailing edge will be needed, so as not to make the actuator work.

In Table 6.1, the maximum and minimum stress values both for the skin and the compliant mechanism elements are reported. In some cases, in particular in the compliant mechanism elements, stress level close to the aluminum's yield strength are reached. A non-linear solver would be strongly recommended in the analysis in order to get even more realistic results. In addition, the actuation force needed so as to achieve the required downwards deflection is reported.

	Inboard			Outboard		
	Skin stress	Mechanism stress	Actuation force	Skin stress	Mechanism stress	Actuation force
			First validation test			
Max	$160MPa$	$50MPa$	$696N$	$323Mpa$	$499Mpa$	$412N$
Min	$386kPa$	$-64MPa$		$1.5Mpa$	$-446MPa$	
			Second validation test			
Max	$225MPa$	$510MPa$	$350N$	$127MPa$	$509MPa$	$350N$
Min	$818kPa$	$-85MPa$		$614kPa$	$-188MPa$	

Table 6.1: Summary results of the validation studies

Chapter 7

Conclusions

This work has presented the design procedure of a compliant mechanism for a morphing trailing edge highlighting the benefits of such technology and drivers that could lead to its final implementation in a real medium-range aircraft. It has been demonstrated how design parameters can be tuned in order to get a trade-off solution in terms of deformation close to the target shape, stress level, actuation force and load-carrying capability.

Throughout the optimization procedure, that has covered from a single objective optimization to a 3D validation study of several solutions in the SARISTU reference wing, it has been seen the improvement achieved from the initial configuration that considered a clamped trailing edge made of a single material to the more sophisticated final configuration in which a solution based on a more flexible material for the skin and a slider placed in the lower skin was exploited.

Nevertheless, it also has been demonstrated that not in all the cases optimal results can be found, like for instance in outboard region. In this case its intrinsic peculiarities like the more slender shape and its more aggressive shape change make its design more critical.

Finally, by performing several 3D validation studies it has been checked the results coming from the multiobjective optimization procedure not only in terms of deformations achieved but also in terms of load-carrying capability of the compliant structure. High connectivity of the solution is crucial for succeeding in having good behavior in both situations.

In principle, compliant mechanism can be applied to very general morphing airfoils or intelligent structures. However, the idea based on a traditional wing box

equipped with morphing leading and trailing edge, better known as conformable or gapless control surfaces, represent a smooth transition between classical aircraft wings and more sophisticated fully-morphing wings. Besides, this solution solves the problem of where to allocate the fuel within a fully-morphing wing together with the fact that offers a competitive strength-to-weight ratio.

7.1 Future developments

The first development should come from the necessity to open the structure in the lower skin so as to get deformation shapes close to the target ones and to avoid high stress levels or buckling. To this aim a solution based on an active slider which allows the horizontal displacement when demanded should be investigated.

Besides, more target shapes and load conditions should be added in the multiobjective optimization. By doing so, a fully adaptive solution could be found improving the aerodynamic performance in more than one flight condition.

These studies should be carried out as well for the other morphing configurations given by SARISTU, where a wider morphing trailing edge in chord-wise direction is considered. This issue could help in finding a more connective solution, which as it has been seen gives a better control in the shape change and a better fulfillment of the structural requirement. Besides, regarding the structural requirement, as already said. a blocking system would be necessary in order not to make the actuator work.

Evidently, all these studies are useless without the correlation of experimental results, since it cannot be forgotten that the expectations are implementing a compliant solution in a real aircraft wing in order to improve its aerodynamic performances.

Finally, the same studies and developments should be performed for the leading edge, being in this case unnecessary to open the structure at any point.

Bibliography

[1] Cavagna, L., Ricci, S and Riccobene, L. *"Application of Adaptive Compliant Mechanism to Morphing Wings,"* Applied Vehicle Technology (AVT-168) Symposium of Morphing Vehicles, NATO Research and Technology Organisation (RTO), Lisbon, Portugal, 20-24 April 2009.

[2] Alessandro De Gaspari. *"A Two Levels Approach for the Optimal Design of Morphing Wings Based On Compliant Structures,"* PhD thesis, Dipartimento di Ingegneria Aerospaziale, Politecnico di Milano, 2010.

[3] Alessandro De Gaspari and Sergio Ricci. *"A two-level approach for the optimal design of morphing wings based on compliant structures"*. Journal of Intelligent Material Systems and Structures, 22:1091–1111, July 2011.

[4] Brenda M. Kulfan. *"Universal parametric geometry representation method"*. Journal of Aircraft, 45(1), January–February 2008.

[5] Brenda Kulfan. *"New supersonic wing far-field composite-element wave-drag optimization method"*. Journal of Aircraft, 46(5), September–October 2009.

[6] Spillman, J. J.,*"The use of variable camber to reduce drag, weight and costs of transport aircraft,"* Aeronautical Journal, January 1992, pp. 1–9.

[7] *"The design of morphing aircraft,"* `http://www.aer.bris.ac.uk/research/morphing/morph-main.html`, 2007, Aerospace Department, University of Bristol.

[8] Vio, G., Marques, S., Cooper, J., and Badcock, K., *"Adaptive aeroelastic concept applied to a civil jet aircraft model,"* AIAA 2010-2991, 51st AIAA/ASME/ASCE/AHS/ASC Structures, Structural Dynamics and Materials (SDM) Conference, Orlando, Florida, April 2010.

[9] Pendleton, E., Bessette, D., Field, P., Miller, G., and Griffin, K., *"Active Aeroelastic Wing Flight Research Program: Technical Program and Model Analytical Development,"* Journal of Aircraft, Vol. 37, No. 4, 2000, pp. 554–561.

[10] Pendleton, E., Flick, P., Paul, D., Voracek, D., and Reichenbach, E., *"The X-53 a summary of the active aeroelastic wing flight research program,"* AIAA 2007, 48th AIAA/ASME/ASCE/AHS/ASC Structures, Structural Dynamics and Materials (SDM) Conference, Honolulu, Hawaii, 2007.

[11] Roth, B. and Crossley, W., *"Applications of optimization techniques in the conceptual design of morphing aircrafts,"* AIAA 2003, Third Annual Aviation Technology, Integration and Operations (ATIO), Denver, Colorado, 2003.

[12] Roth, B., Peters, C. and Crossley, W., *"Aircraft sizing with morphing as ab independent variable: motivation, strategies and investigations."* AIAA 2007, 48th AIAA/ASME/ASCE/AHS/ASC Structures, Structural Dynamics and Materials (SDM) Conference, Honolulu, Hawaii, 2007.

[13] Ghiringhelli, G. L., Masarati, P., and Mantegazza, P., *"Multibody Implementation of Finite Volume C^0 Beams,"* AIAA Journal, Vol. 38, No. 1, January 2000.

[14] Masarati, P. and Mantegazza, P., *"On the C^0 discretization of beams by finite elements and finite volume,"* Aerotecnica Missili e Spazio, Vol. 75, 1997, pp. 77–86.

[15] Monner, H. P., *"Realization of an Optimized Wing Camber by using Formvariable Flap Structures,"* Aerospace Science Technology, Vol. 5, 2001, pp. 445–455.

[16] Sater, J. M., Crowe, C. R., Antcliff, R., and Das, A., *"Smart Air and Space Structures,"* Structures Technology for Future Aerospace Systems, edited by A. K. Noor and P. Zarchan, Vol. 188, chap. 6, AIAA, 2000, pp. 269–335.

[17] Monner, H. P., Kintscher, M., Lorkowski, T., and Storm, S., *"Design of a Smart Droop Nose as Leading Edge High Lift System for Transportation Aircrafts,"* AIAA 2009–2128, 50th AIAA/ASME/ ASCE/AHS/ASC Structures, Structural Dynamics and Materials (SDM) Conference, Palm Springs, California, 4–7 May 2009.

[18] Kota, S., Osborn, R., Ervin, G., Maric, D., Flick, P., and Paul, D., *"Mission Adaptive Compliant Wing - Design, Fabrication and Flight Test,"* Applied Vehicle Technology

(AVT-168) Symposium on Morphing Vehicles, NATO Research and Technology Organisation (RTO), Lisbon, Portugal, 20–24 April 2009, pp. 1–20.

[19] Ricci, S. and Terraneo, M., *"Design, Manufacturing and Preliminary Test Results of an Adaptive Wing Camber Model,"* 47th AIAA/ASME/ ASCE/AHS/ASC Structures, Structural Dynamics and Materials (SDM) Conference, Newport, Rhode Island, 1–4 May 2006.

[20] Brenda M. Kulfan. *"fundamental" parametric geometry representations for aircraft component shapes*. Portsmouth, Virginia, 6-8 September 2006. 11th AIAA/ISSMO Multidisciplinary Analysis and Optimization Conference.

[21] Shield, R. T. and Prager, W., *"Optimal Structural Design for Given Deflection,"* Journal of Applied Mathematics and Physics, ZAMP, Vol. 21, 1970, pp. 513–523.

[22] Alessandro De Gaspari and Sergio Ricci. *"A Parametric Framework for the Design of Morphing Wings"*. 6th ECCOMAS Conference on Smart Materials, SMART2013. Politecnico di Torino, 24-26 June 2013.

[23] Sigmund, O. and Bendsøe, M. P., *"Topology Optimization: Theory, Methods and Applications,"* Springer, 2003.

[24] Martínez, P., Martí, P., and Querin, O. M., *"Growth Method for Size, Topology and Geometry Optimization of Truss Structures,"* Structural and Multidisciplinary Optimization, Vol. 33, No. 1, 2007, pp. 13–26.

[25] Deb, K. *"Multi-Objective Optimization using Evolutionary Algorithms,"* Wiley, 2009.